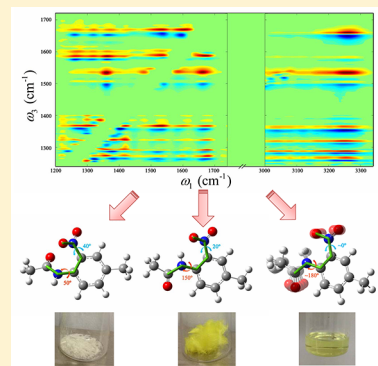


Vibrational Cross-Angles in Condensed Molecules: A Structural Tool

Hailong Chen,[†] Yufan Zhang,[†] Jiebo Li,[†] Hongjun Liu,[‡] De-En Jiang,[‡] and Junrong Zheng^{*,†}[†]Department of Chemistry, Rice University, Houston, Texas 77005, United States[‡]Chemical Sciences Division, Oak Ridge National Laboratory, Oak Ridge, Tennessee 37831, United States

S Supporting Information

ABSTRACT: The fluctuations of three-dimensional molecular conformations of a molecule in different environments play critical roles in many important chemical and biological processes. X-ray diffraction (XRD) techniques and nuclear magnetic resonance (NMR) methods are routinely applied to monitor the molecular conformations in condensed phases. However, some special requirements of the methods have prevented them from exploring many molecular phenomena at the current stage. Here, we introduce another method to resolve molecular conformations based on an ultrafast MIR/T-Hz multiple-dimensional vibrational spectroscopic technique. The model molecule (4'-methyl-2'-nitroacetanilide, MNA) is prepared in two of its crystalline forms and liquid samples. Two polarized ultrafast infrared pulses are then used to determine the cross-angles of vibrational transition moment directions by exciting one vibrational band and detecting the induced response on another vibrational band of the molecule. The vibrational cross-angles are then converted into molecular conformations with the aid of calculations. The molecular conformations determined by the method are supported by X-ray diffraction and molecular dynamics simulation results. The experimental results suggest that thermodynamic interactions with solvent molecules are not altering the molecular conformations of MNA in the solutions to control their ultimate conformations in the crystals.



1. INTRODUCTION

In condensed phases, noncovalent interactions, including intramolecular forces between different parts of a flexible molecule and intermolecular interactions, can often strain a molecule into conformations that are not favorable for the isolated molecule.

The ability to form such interconvertible strained conformations of a molecule in different environments plays critical roles in many important chemical and biological phenomena, e.g., the selectivity of chemical reactions, protein foldings, molecular recognitions, the fusion of biological membranes, and the formation of polymorphs of pharmaceutical drugs.^{1–8} The conformational fluctuations of a molecule are caused by the rotations of different parts of the molecule about its single bonds (σ bonds), e.g., C–C, C–O, and C–N single bonds. One simple example is the interconversion of cis/trans conformations of a disubstituted ethane molecule, which occurs within tens of picoseconds (ps, 10^{-12} s) in a room temperature liquid.⁹ In a more complex molecule there are many possible conformations arising from internal rotation about several (or many) single bonds similar to this cis/trans isomerization. Tremendous efforts have been devoted to develop tools to monitor real time three-dimensional (3D) molecular conformations and structures seeking to understand the correlations between molecular structures and functions at different time scales. Among many tools developed, X-ray diffraction techniques and nuclear magnetic resonance (NMR) methods are among the most successful ones. However, at the current stage, some molecular structures and conformations are difficult to be resolved by the two methods because of some of

their special characteristics or general availability,^{10,11} e.g., the relatively broad linewidths of solid-state NMR, the sensitivity to molecular magnetic properties, and the relatively small X-ray diffraction (XRD) cross-section of H atom.

Here, we discuss an approach using an ultrafast ($\leq 10^{-12}$ second) nonlinear MIR/T-Hz (mid-infrared/tera-Hz) vibrational technique,^{12,13} which can potentially address some systems that the two traditional tools at the current stage may have difficulties with as a structural tool to determine molecular conformations by measuring the relative directions of transition moments of different vibrational modes.^{12,13} In this way, the cross-angle between the transition moment directions of two vibrational bands can be experimentally determined between 0° to 90° (if the angle is greater than 90° , its supplement is determined).^{13–15} Because vibrational cross-angles are extremely sensitive to the directionality of chemical bonds in the molecule,¹⁶ which can be checked by ab initio calculations, they can be translated into cross-angles among chemical bonds. The 3D molecular conformation can then be constructed based on the chemical bond cross-angles. In our previous publications, we found some signs that the approach can work in liquids and solids and on the surfaces of metal nanoparticles.^{17,18} However, the method has not been benchmarked with standard mature experimental techniques because of the difficulties of applying the traditional techniques to these situations. In this work, we first use the structures of

Received: June 26, 2013

Revised: August 7, 2013

Published: August 12, 2013

two crystalline polymorphs of an organic molecule, 4'-methyl-2'-nitroacetanilide (MNA), determined by XRD to benchmark the method and then present its conformations in the melt state and liquid solutions determined by this method. The determined molecular conformations in liquids are then compared to the results from molecular dynamics simulations.

2. EXPERIMENTS AND METHODS

As shown in Figure S1, Supporting Information, a ps amplifier and a fs amplifier are synchronized with the same seed pulse from an oscillator. The ps amplifier pumps an OPA (optical parametric amplifier) to produce ~ 0.8 ps (vary from 0.7–0.9 ps in different frequencies). Mid-IR pulses with a bandwidth 10–35 cm^{-1} in a tunable frequency range from 400 to 4000 cm^{-1} with energy 1–40 $\mu\text{J}/\text{pulse}$ (1–10 $\mu\text{J}/\text{pulse}$ for 400 to 900 cm^{-1} and >10 $\mu\text{J}/\text{pulse}$ for higher frequencies) at 1 kHz. Light from the fs amplifier is used to generate a high-intensity mid-IR and terahertz supercontinuum pulse. Specifically, the collimated 800 nm beam from the fs amplifier is frequency-doubled by passing through a Type-I 150 μm thick BBO crystal cut at 29.2° to generate a 400 nm pulse. A dual wave plate is used to tune the relative polarizations of the 800 and 400 nm pulses, which operates as a full-wave plate at 400 nm and a half-wave plate at 800 nm. Temporal walkoff between two beams is compensated by inserting a 2 mm thick BBO (cut at 55°) between the doubling crystal and the wave plate, where the 800 and 400 nm pulses propagate with orthogonal polarizations with different velocities in the delay plate.^{19,20} The supercontinuum pulse is then generated by focusing the two copropagating beams on air, with a pulse duration around 110 fs in the frequency range from <20 to >3500 cm^{-1} at 1 kHz (Figure S1 in the Supporting Information), and the shot to shot fluctuation is less than 1% in most of the spectral region.

In the nonlinear IR experiments, the ps IR pulse is the excitation beam (the excitation power is adjusted based on need, and the interaction spot varies from 100 to 500 μm). The supercontinuum pulse is the detection beam, which is frequency-resolved by a spectrograph (resolution is 1–3 cm^{-1} dependent on the frequency) yielding the detection axis of a 2D IR spectrum. Scanning the excitation frequency yields the other axis of the spectrum. Two polarizers are added into the detection beam path to selectively measure the parallel or perpendicular polarized signal relative to the excitation beam. The whole setup included frequency tuning is computer controlled.

MNA was purchased from Aldrich, and its two crystal polymorphs were prepared according to the literature.²¹ The white form was produced by cooling a saturated MNA solution in a water/ethanol mixture (1/3 volume ratio), and the yellow crystal was grown from saturated MNA solutions in hexane or CCl_4 . The crystals were mixed with KBr and compressed into pellets for optical measurements. For the solution samples, the MNA in aqueous ethanolic solvent was measured at 65°C with the concentration about 2 M (supersaturated, cooled down from the saturated solution at 70°C), and CCl_4 solutions were measured at room temperature (21°C) with the concentration about 0.3 M (saturated solution) and 0.01 M (dilute solution), respectively. The melt form of MNA was measured at 100°C (the melting range for MNA is 91 – 96°C). All the experiments conducted at high temperature were achieved by a temperature controller connected with separate heater and sample thermocouples.

Density functional theory (DFT) calculations were used to convert atomic coordinates (relative atomic orientations) into vibrational coordinates (relative vibrational orientations). In this work, the DFT calculations were carried out using Gaussian09. The level and basis set used were Becke's 3-parameter hybrid functional combined with the Lee–Yang–Parr correction functional, abbreviated as B3LYP, and 6-311++G(d,p). The transition dipole moment directions of molecules in CCl_4 solvent were calculated by using the conductor-like polarizable continuum model (CPCM). To calculate the vibrational cross-angles for each conformation, we fixed the two dihedral angles ($\angle\text{CC}/\text{NO}$ and $\angle\text{CC}/\text{NC}$) with preset values, and the other degrees of freedom were optimized by the calculations. In the samples, all torsion angles of two methyl groups are significantly populated, but in calculations based on the energy minimum only one torsion angle is chosen for each conformation. This can cause some uncertainty in Er (defined in eq 2). However, the uncertainty is negligible (only $\sim 0.1^\circ$) because the 15 dihedral angles used are not sensitive to the torsion angles of methyl groups and the methyl torsion angles at the energy minima are very close to the average most probable methyl torsion angles, see Figure S4, Supporting Information. It is well-known that the transition dipole directions of a vibrational mode at the H-bonded state and the free state can be very different. It seems that the calculated directions from the H-bonded species should be used for samples in which the molecules are H-bonded. **This turns out to be not true.** The reason is that the experimental cross-peak intensity is mainly from the local vibrational coupling. In other words, the intramolecular coupling dominates over the intermolecular interactions. As we have demonstrated, the cross-peak intensity from the intramolecular coupling between a combination band and the CN stretch of SCN^- is much stronger than that of the cross-peak between the OD stretch and the CN stretch of SCN^- in a $\text{KSCN}/\text{D}_2\text{O}$ solution where SCN^- is believed to form a strong H-bond with D_2O .¹² Therefore, using the calculated delocalized transition dipole directions from a H-bonded species to analyze the experimental results will cause a big error, as we have tested for the previous systems.¹⁸ To avoid this problem, we first optimized the structure of a H-bonded molecule with a H-bonded partner, and then calculated the vibrational transition dipole directions of this molecule with the H-bonded structure but without the H-bonded partner. In this way, the structure of the molecule is H-bonded, but the transition dipole directions are localized within the molecule because the H-bonded partner is not involved in the direction calculations. In practice, we found that results through this procedure are not significantly different from those by directly calculating the isolated nonbonded molecule, probably because the H-bond does not change the molecular structure significantly. In addition, as demonstrated, the calculated transition dipole directions of relatively localized modes with different calculation levels are very similar.¹⁶

Force field parameters for MNA, CCl_4 , and ethanol were adapted from the general Amber force field²² (GAFF) except for partial charges and dihedrals of interest (CCNO and CCNC in MNA). The partial charges were determined using the restrained electrostatic potential (RESP) method²³ at the B3LYP/6-31G(d) level. Parameters for CCNO and CCNC dihedrals in MNA were refined so as to be able to accurately reproduce the gas-phase potential energy surfaces of the two dihedrals computed at the MP2/aug-cc-pVDZ level.²⁴ The TIP3P model for water²⁵ was used.

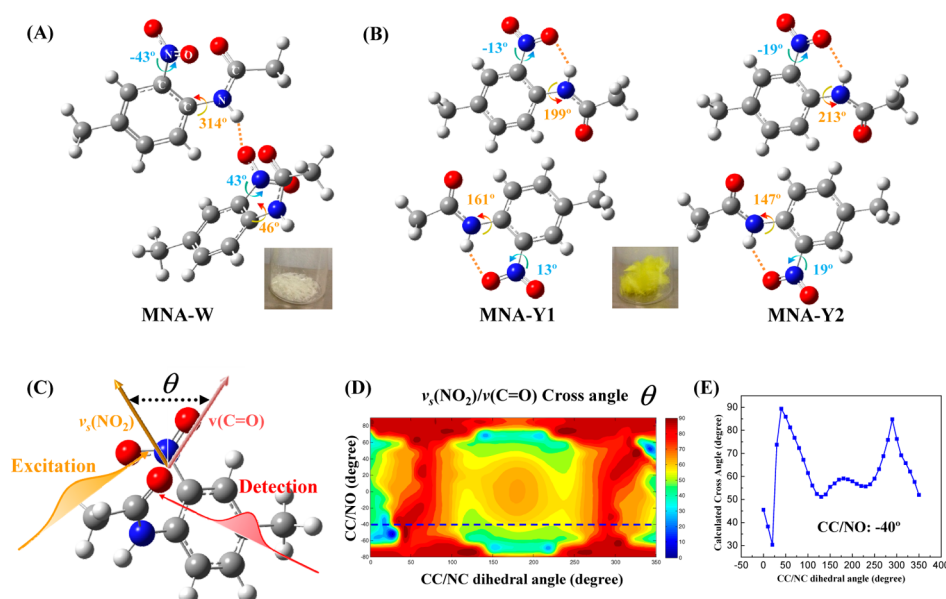


Figure 1. Molecular conformations of MNA in (A) the white crystal and (B) in the yellow crystal. (C) Illustration of how the vibrational cross-angle between two modes is experimentally determined. (D) Calculated vibrational cross-angle between the NO₂ symmetric stretch and the C=O stretch of different MNA conformations with various $\angle\text{CC}/\text{NO}$ and $\angle\text{CC}/\text{NC}$ dihedral angles. The z-axis (intensity) is the vibrational cross-angle θ . (E) Calculated vibrational cross-angle between the NO₂ stretch and the C=O stretch of different MNA conformations with various $\angle\text{CC}/\text{NC}$ dihedral angles with a fixed $\angle\text{CC}/\text{NO} = -40^\circ$. The results indicate that the correlation between one vibrational cross-angle and one bond dihedral angle is not one-to-one.

MD simulations for the MNA melt at 400 K (100 MNA); 0.3 M MNA in CCl₄ at 298 K (20 MNA in 344 CCl₄) and 2.0 M MNA in water/ethanol (3:1 volume) at 338 K (20 MNA in the mixture of 185 H₂O and 171 CH₃CH₂OH) were carried out using the LAMMPS package.²⁶ The Nose–Hoover thermostat and barostat were used to keep constant pressure of 1 bar and constant temperature.²⁷ After a proper equilibration, a trajectory of 5 ns production run was used for the statistical analysis of the two dihedrals of interest.

3. RESULTS AND DISCUSSION

3.1. Molecular Conformations of MNA in the White and Yellow Crystals. MNA can form a white crystal from a water/ethanol mixed solution and a yellow crystal from its solutions in nonpolar solvents.²⁸ The molecular conformations in these two crystals have been characterized with XRD²⁹ and are displayed in Figure 1. The MNA conformations are determined by the angles between three molecular planes: the benzene plane, the nitro plane, and the amide plane. In the crystals, the hydrogen of the amide group can either form one hydrogen bond with one oxygen of the nitro group within the same molecule or it can take part in a hydrogen bond between two adjacent molecules. In the white crystal (MNA-W, Figure 1A), intermolecular H-bonds dominate, and the nitro and amide planes are tilted from the benzene plane at very large angles. This noncoplanar structure of MNA leads to the coexistence of two chiral structures in equal amounts in the crystal. The dihedral angle between the benzene plane and the nitro plane $\angle\text{CC}/\text{NO}$ of one chiral image is 43° , and that between the benzene plane and the amide plane $\angle\text{CC}/\text{NC}$ is 46° . For the other chirality, the dihedral angles are -43° and -46° (314°). In the yellow crystal (Figure 1B), intramolecular H-bonds dominate. The three planes are still noncoplanar but with much smaller tilted angles. Two nonequivalent molecules with slightly different structures are present in the unit cell. We

will name these two molecules MNA-Y1 and MNA-Y2, each of which contains two chiral images of equal amounts. In MNA-Y1, the dihedral angles $\angle\text{CC}/\text{NO}$ and $\angle\text{CC}/\text{NC}$ of one chiral image are 13° and 161° , respectively, and -13° and -161° (199°) for the other chiral image. In MNA-Y2, the dihedral angles $\angle\text{CC}/\text{NO}$ and $\angle\text{CC}/\text{NC}$ are 19° and 147° , respectively, for one chiral image, and -19° and -147° (213°) for the other chiral image. The torsion angles of the two methyl groups are undetermined by XRD at room temperature because each angle is significantly populated due to the low rotational barriers (0.6–1.2 kcal/mol from calculations, in Figures S3 and S4 of the Supporting Information. More discussions about the results on this type of torsion angle by the vibrational cross-angle method are also provided therein).

3.2. Determine MNA Molecular Conformations in the White Crystal. To experimentally determine the dihedral angles that define the relative orientations of the three planes in MNA by the vibrational transition moment cross-angle method, we first measure the cross-angles among vibrational modes that are sensitive to the changes of the dihedral angles $\angle\text{CC}/\text{NO}$ and $\angle\text{CC}/\text{NC}$. As illustrated in Figure 1C, a linearly polarized IR pulse excites a vibrational mode (the NO₂ stretch at 1362 cm^{-1}). After a very short period of time (0.1–0.2 ps) before the molecular rotation or conformational changes have occurred for a substantial extent, another linearly polarized pulse of different frequencies detects a signal generated from the response of another vibrational mode (the C=O stretch) to the excitation of the NO₂ stretch. In general, the excitation of one vibrational mode can lead to the vibrational frequency shift of another mode because of the anharmonic coupling.³⁰ The coupling produces a cross-peak pair in the experimental results as displayed in Figure 2B. In Figure 2B, the excitation frequency $\omega_1 = 1362\text{ cm}^{-1}$ is the NO₂ symmetric stretch 0–1 transition frequency, indicating that the cross-peak pair is from the NO₂ excitation. The detection frequency (red peak) $\omega_3 = 1672\text{ cm}^{-1}$

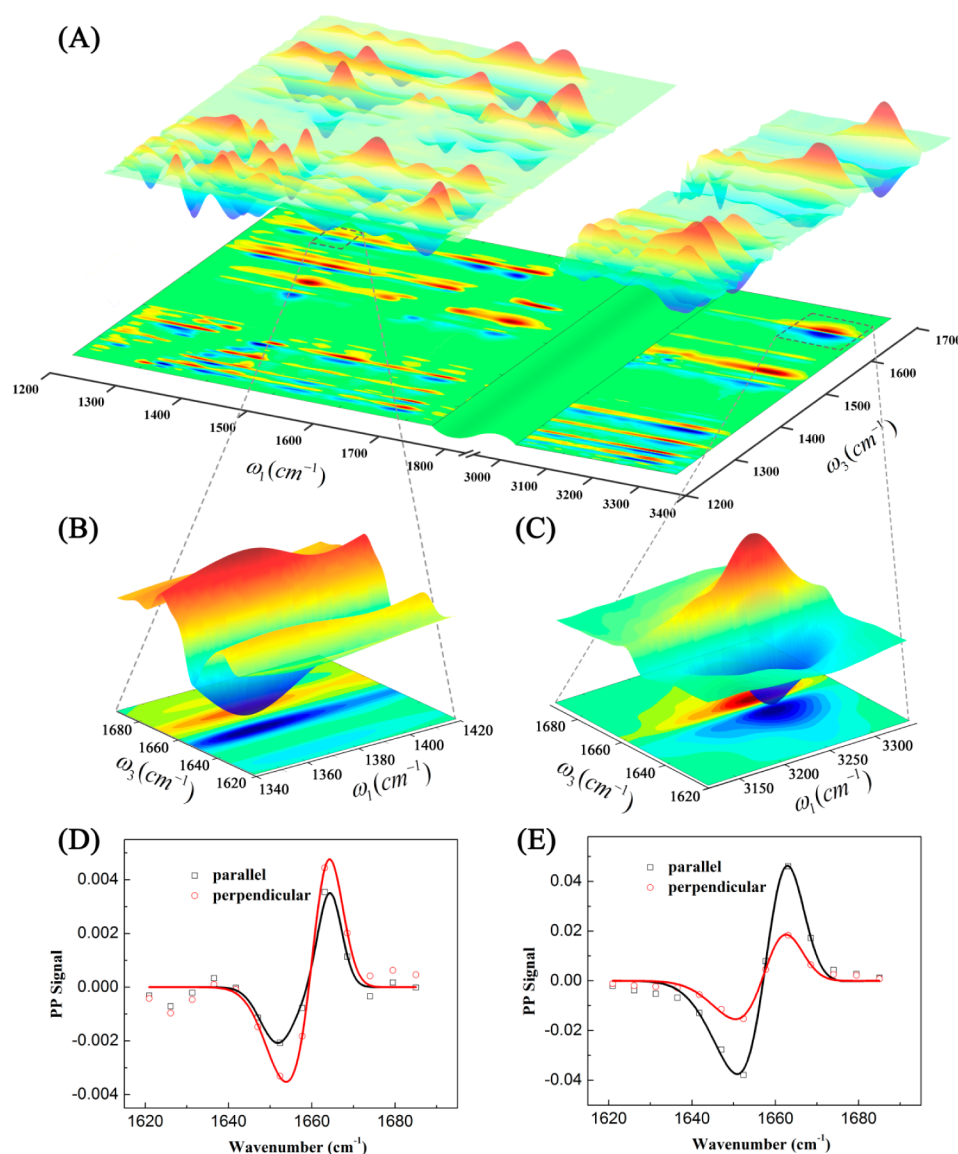


Figure 2. (A) Multiple-mode 2D IR spectrum of a polycrystalline sample of the MNA white crystal at waiting time 0.2 ps with the detection beam perpendicular to the excitation beam. The relative intensities of peaks are adjusted to be comparably visible by multiplying the raw data with constants, which are listed in the Supporting Information. (B) Enlarged 2D-IR spectrum for the cross-peak pair between $\nu_s(\text{NO}_2)$ (ω_1) and $\nu(\text{C}=\text{O})$ (ω_3), and (C) enlarged 2D-IR spectrum for the cross-peak pair between $\nu(\text{NH})$ (ω_1) and $\nu(\text{C}=\text{O})$ (ω_3) frequency range. (D) A slice cut along $\omega_1 = 1362 \text{ cm}^{-1}$ of panel B with the polarization of the excitation both parallel (\parallel) and perpendicular (\perp) to the polarization of the detection beam. (E) A slice cut along $\omega_1 = 3260 \text{ cm}^{-1}$ of panel C with the polarization of the excitation both parallel (\parallel) and perpendicular (\perp) to the polarization of the detection beam. The solid lines denote Gaussian peak fits. Because the vibrational cross-angles are different, the relative intensities of the parallel and perpendicular signals are very different in panels D and E.

is the C=O stretch 0–1 transition frequency, indicating that the cross-peak pair is from the 0–1 transition frequency shift of the C=O stretch from 1672 (red peak) to 1655 cm^{-1} (blue peak) caused by the NO_2 excitation. The amplitudes of the cross-peaks (Figure 2D) are dependent on the polarizations of the exciting and detecting beams, and the cross-angle θ between the transition dipole moment directions of the two coupled modes. For a sample isotropically distributed within the laser focus spot (diameter $\approx 150 \mu\text{m}$), the vibration cross-angle can be straightforwardly determined based on the following relationship:^{13,31}

$$\frac{I_{\perp}}{I_{\parallel}} = \frac{2 - \cos^2 \theta}{1 + 2 \cos^2 \theta} \quad (1)$$

where I_{\parallel} and I_{\perp} are cross-peak intensities with parallel and perpendicular excitation/detection polarizations, respectively. θ is the transition dipole moment cross-angle between two coupled modes. From both parallel and perpendicular measurements (Figure 2D) and eq 1, the vibrational cross-angle between the NO_2 stretch and the C=O stretch is determined to be $70^{\circ} \pm 2^{\circ}$.

It is important to note that the derivation of eq 1 requires samples within the laser focus spot to be isotropic.^{12,13} The cross-peaks used for the vibrational cross-angle analysis can come from four origins: vibrational couplings, direct vibrational energy transfers, the relaxation-induced heat effects, and chemical exchange.¹³ At very short waiting times before any chemical transformations or rotations or intermolecular energy (or heat) exchanges have occurred for a noticeable amount,

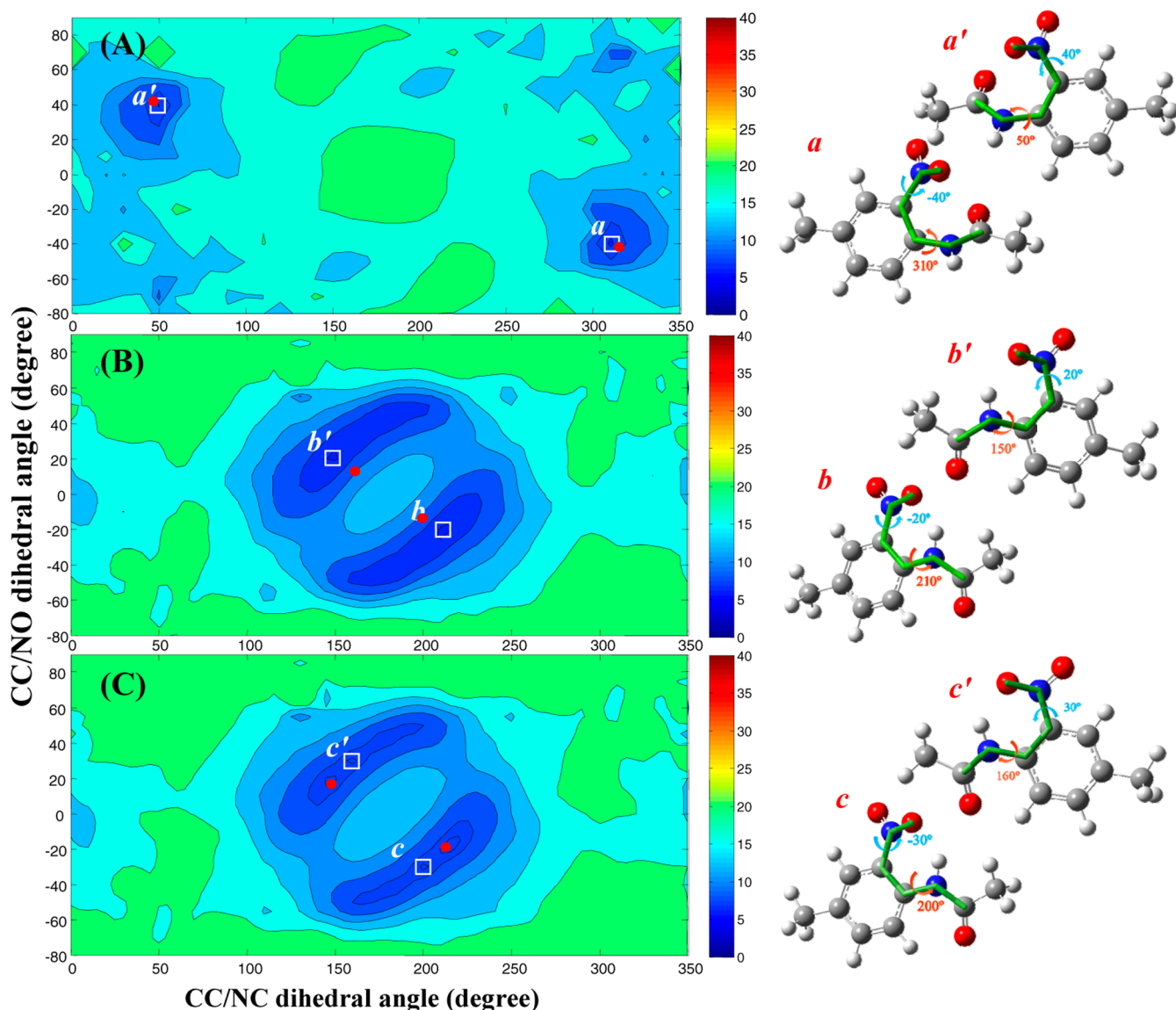


Figure 3. Average difference E_r between the experimental and calculated vibrational cross-angles of MNA conformations with different $\angle\text{CC}/\text{NO}$ and $\angle\text{CC}/\text{NC}$ dihedral angles for (A) MNA-W, (B) MNA-Y1, and (C) MNA-Y2. The z-axis is the amplitude of E_r . The minimum E_r values of each MNA species are labeled with white boxes, which correspond to the most possible molecular conformations in the crystal, as depicted in the right panels. The dihedral angles of red dots are determined by XRD.

cross-angles from the first three origins (couplings, intramolecular energy transfers, and heat effects) can be used to analyze the vibrational cross-angles by applying eq 1.¹² Cross-peaks because of chemical exchanges are typically from the same vibrational modes of the same molecule under different situations. Their anisotropies reflect the structural changes of the molecule in different environments, not the cross-angle between two coupled modes. Experimentally, the cross-peaks from chemical exchanges can be easily distinguished from those of the other three origins based on the molecular structures, vibrational frequencies, and waiting times.¹³ Another issue of the method is that there is always a temporal uncertainty about 100–200 fs. Some small molecules in environments with low viscosities can rotate for some degrees within such a period, which can cause some uncertainty in the vibrational cross-angle determination. The uncertainty range can be estimated and compensated by measuring the waiting time-dependent anisotropies of both diagonal and cross-peaks of the same

molecule. One last issue is that the experimental uncertainty across the entire vibrational cross-angle range ($0\text{--}90^\circ$) is not linearly distributed. At $\sim 45^\circ$, the uncertainty is relatively small, and at $\sim 0^\circ$ and 90° , the uncertainties are relatively large.¹³ Some weighing factors based on the different uncertainties can be added into the analysis to improve the accuracy of the final results.

The next step is to convert the measured vibrational cross-angle into the chemical bond dihedral angles. As displayed in Figure 1D, the calculated vibrational cross-angle θ between the NO_2 stretch and the $\text{C}=\text{O}$ stretch is very sensitive to the changes of the two dihedral angles. With the change of the dihedral angles from 0° to 360° , θ varies across the entire range from 0° to 90° . However, the correspondence between the bond dihedral angles and the vibrational cross-angle θ is not one-to-one. Even with a fixed $\angle\text{CC}/\text{NO} = -40^\circ$, on average about four $\angle\text{CC}/\text{NC}$ angles give the same θ (Figure 1E). The **non-one-to-one correspondence suggests that, in order to**

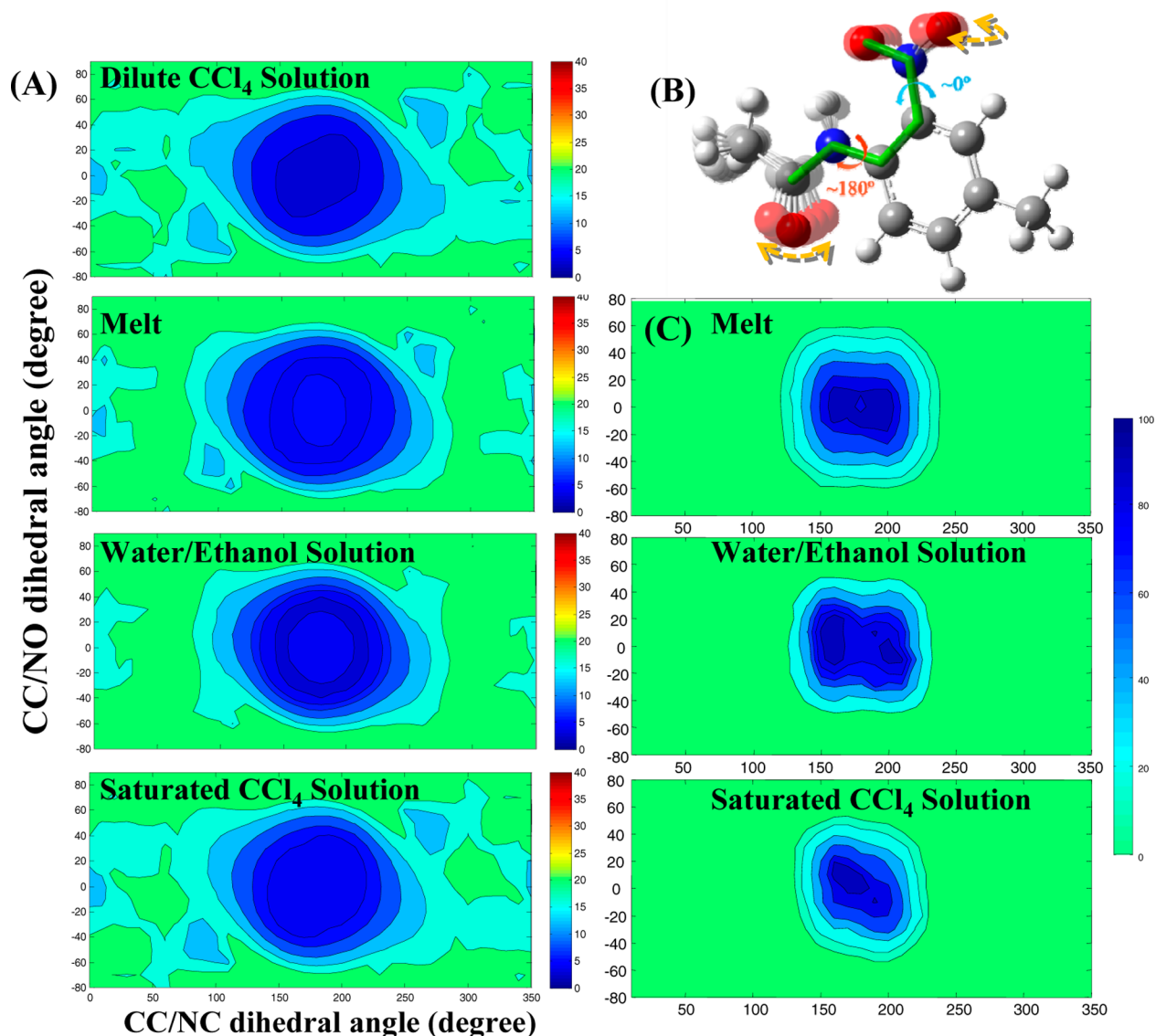


Figure 4. (A) Average difference Er between the experimental and calculated vibrational cross-angles of MNA conformations with different $\angle CC/NO$ and $\angle CC/NC$ dihedral angles for the four liquid samples. The z -axis is the amplitude of Er . (B) The MNA molecular conformation corresponding to the dihedral angles of the Er minima in all four liquid samples. (C) Conformational distributions of liquid samples 2–4 from MD simulations. The z -axis is the relative population of each conformation with a pair of $\angle CC/NC$ and $\angle CC/NO$ dihedral angles as the x - and y -axis.

obtain a single value for any bond dihedral angle, a sufficiently large number of vibrational cross-angles of which the dihedral-angle dependences are different from each other must be simultaneously measured. We therefore scanned the vibrational cross-angles among modes of frequencies from 1200 to 3400 cm^{-1} . The spectral data are plotted in Figure 2A. From the data, we select 15 cross-peak pairs of vibrational modes, which have relatively little spectral overlap and are associated with CH, NO_2 , C=O, C=C, and NH stretches corresponding to 15 vibrational cross-angles that have different dihedral-angle dependences (the details of the 15 pairs of vibrational modes are provided in the Supporting Information) to derive the dihedral angles $\angle CC/NO$ and $\angle CC/NC$ for the white crystal. The dihedral angles can be obtained from the experimental vibrational cross-angles with the aid of the equation

$$Er = \frac{\sum_{i=1}^m |A_i^C - A_i^E|}{m} \quad (2)$$

where A_i^C is the calculated vibrational cross-angle of the i th pair of normal modes of a molecular conformation with a pair values (x_i, y_i) of dihedral angles $(\angle CC/NC, \angle CC/NO)$. A_i^E is the experimental vibrational cross-angle of the i th pair of normal modes (detailed results are listed in Table S3, Supporting Information), and m is the number of pairs. The dihedral angle values (x_m, y_m) of the conformation, which gives the smallest Er , are the most probable angles determined by the method.

We calculated the 15 vibrational cross-angles for each of 648 MNA conformations, which are constructed by varying the dihedral angle $\angle CC/NC$ from 0° to 350° and $\angle CC/NO$ from -80° to 90° (because of the symmetry of the nitro group, a variation range of 180° is sufficient) for every 10° . The 15 calculated vibrational cross-angles from each of the conformations are compared to the experimental results. The average

difference Er defined by eq 2 between the calculated and experimental vibrational cross-angles versus the two dihedral angles is plotted in Figure 3A. Two global minima of Er at the dihedral angles ($\angle CC/NC$, $\angle CC/NO$) around (50° , 40°) and (310° , -40°) are clearly visible. The molecular conformations with dihedral angles in these two minima are the most probable conformations in the white crystal, depicted in the right panel of Figure 3A. The dihedral angles determined from the vibrational transition moment cross-angle method are very close to those ($(46^\circ$, $43^\circ)$ and (314° , -43°)) determined by XRD (red dots in Figure 3A).

Different from the vibrational cross-angle method demonstrated here, no clear correlation between the vibrational frequencies and molecular conformations can be found by using eq 2 to obtain the average difference Ers for calculated and experimental vibrational frequencies. Results are displayed in Figure S19 in the Supporting Information.

3.3. Determine MNA Molecular Conformations in the Yellow Crystal. The yellow crystal is the mixture of two different species MNA-Y1 and MNA-Y2. Following the method described above for the white crystal to analyze the yellow crystal gives only the average of MNA-Y1 and MNA-Y2. A different approach is needed to resolve the individual conformation of these two species in the same sample. The NH stretch frequency (3360 cm^{-1}) and the C=O stretch frequency (1709 cm^{-1}) of MNA-Y1 are different from those (3383 and 1720 cm^{-1}) of MNA-Y2 (FTIR spectra are displayed in the Supporting Information). Because of the frequency differences and the fact that the cross-peaks are mainly contributed from the intramolecular vibrational coupling,¹² the vibrational cross-angles associated with these two vibrational modes can be unambiguously assigned to either MNA-Y1 or MNA-Y2. These vibrational cross-angles can then be used to determine the individual conformations of MNA-Y1 and MNA-Y2. Following this strategy, for each species, eight vibrational cross-angles associated with either the NH stretch or the C=O stretch in addition to four other cross-angles (the details of these modes are listed in the Supporting Information) were selected to analyze the conformations of these two species. The average difference Er between these experimental vibrational cross-angles and the calculated cross-angles vs the dihedral angles is plotted in Figure 3B for MNA-Y1 and Figure 3C for MNA-Y2. For MNA-Y1, the dihedral angles ($\angle CC/NC$, $\angle CC/NO$) determined from Figure 3B are (150° , 20°) and (210° , -20°), and those for MNA-Y2 from Figure 3C are (160° , 30°) and (200° , -30°). Similar to the case of the white crystal, these results are also very close to the structures determined by XRD (red dots in Figure 3B,C). The difference in the dihedral angles determined by the two methods is about 10 – 20° .

3.4. Molecular Conformations of MNA in Liquids. As described above, the MNA molecular conformations are highly different in the white and yellow crystals grown from solutions of different solvents. A fundamental question associated with the formation of polymorphs is how the solvent molecules function in solutions to control the ultimate molecular conformations in crystals: through changing the equilibrium molecular conformations of the solute or modifying the kinetic process of crystallization to selectively facilitate the formation of nuclei for one polymorph or both.³³ To explore this issue, we applied the vibrational cross-angle method to investigate the molecular conformations of MNA in four liquids: sample 1 is a dilute MNA solution in CCl_4 (0.01 M at room temperature), of which the intramolecular H-bond between the nitro group and

the amide group is much stronger than the solute/solvent interaction; sample 2 is MNA in the melt state at 100°C (above the melting points of both crystals), of which both intramolecular and intermolecular H-bonds between the nitro group and the amide group coexist; sample 3 is a supersaturated MNA solution in which no visible particles can be found in a water/ethanol ($1/3$ volume ratio) mixture ($\sim 2\text{ M}$ at 65°C , cooled down from the saturated solution at 70°C), from which the white crystal is grown; and sample 4 is a saturated MNA solution in CCl_4 (0.3 M at room temperature), from which the yellow crystal is grown.

The average difference Ers between the experimental and calculated vibrational cross-angles of MNA conformations with different $\angle CC/NO$ and $\angle CC/NC$ dihedral angles for the four liquid samples are displayed in Figure 4A. The z -axis of the plots is the amplitude of Er . The results of the four liquids in Figure 4A are very similar: the most probable conformations of MNA in the liquids have a broad distribution centered around the coplanar structure of which the dihedral angles are (180° , 0°). The liquid conformations are illustrated in Figure 4B. MD simulations on samples 2–4 give similar results. As displayed in Figure 4C, more than 50% of the conformations of MNA in the three liquids are conformations with the dihedral angles tilted less than 30° from the coplanar structure. The conformations in the liquids are different from those in either crystal. The results show that even in the supersaturated state, the dominant molecular conformations in the solution from which a crystal is grown is very different from those in the crystal and that molecular conformations are very similar in the different solutions with different solvents from which different polymorphs are grown. The experiments suggest that the solvent molecules are not through thermodynamically altering the molecular conformations of MNA but probably through modifying the kinetic process of crystallization to control its ultimate molecular conformations in the crystals.

4. CONCLUDING REMARKS

In summary, we demonstrate that the relative directions of vibrational transition dipole moments can be utilized to determine molecular conformations, providing a molecular structural tool with a temporal resolution 6 orders of magnitude faster than that of NMR. Because of the relative ease of manipulating the laser beams, the flexibility of the sample state (the sample can be crystalline or amorphous powders or single crystals, gels, liquids, or very dense gases), the requirement of relatively small amount of sample ($\sim 10^{-8}\text{ g}$ for organic molecules like MNA), and especially the ultrafast temporal resolution, the method will be relevant to many fields where static or fast fluctuating molecular structures and conformations are important, e.g., heterogeneous catalysis, nonaqueous electrolytes in energy storage devices,³⁴ organic solar cells, and biomembranes. With the extension of laser frequency to the far IR region, the improvement of the calculation strategy, and the accumulation of database for local versus delocalized vibrational couplings to address the spectral overlap problem, the method is expected to be able to resolve conformations of molecules much larger than MNA demonstrated here.

■ ASSOCIATED CONTENT

Supporting Information

Experimental setup; studies on the conformation of methyl group in MNA-W; FTIR spectra and corresponding assignments of some major absorption peaks; polarization-selective

data for all the pairs of coupled vibrational modes of all the samples; dependence of vibrational cross-angles on the conformation; dependence of the average difference E_r on the conformation; time-dependent anisotropy data for the diagonal peak; comparison between the experimental and calculated vibrational frequencies. This material is available free of charge via the Internet at <http://pubs.acs.org>.

AUTHOR INFORMATION

Corresponding Author

*(J.Z.) E-mail: junrong@rice.edu.

Notes

The authors declare no competing financial interest.

ACKNOWLEDGMENTS

This material is based upon work supported by the Air Force Office of Scientific Research under AFOSR Award No. FA9550-11-1-0070, the Welch foundation under Award No. C-1752, and a Packard fellowship to J.Z. Work at ORNL was supported by the Division of Chemical Sciences, Geosciences, and Biosciences, Office of Basic Energy Sciences, U.S. Department of Energy. This research used resources of the National Energy Research Scientific Computing Center (NERSC), which is supported by the Office of Science of the U.S. Department of Energy under contract no. DE-AC02-05CH11231.

REFERENCES

- (1) Tian, P.; Keusters, D.; Suzuki, Y.; Warren, W. S. Femtosecond Phase-Coherent Two-Dimensional Spectroscopy. *Science* **2003**, *300*, 1553–1555.
- (2) DeFlores, L. P.; Ganim, Z.; Nicodemus, R. A.; Tokmakoff, A. Amide I'-II' 2D IR Spectroscopy Provides Enhanced Protein Secondary Structural Sensitivity. *J. Am. Chem. Soc.* **2009**, *131*, 3385–3391.
- (3) Finkelstein, I. J.; Zheng, J. R.; Ishikawa, H.; Kim, S.; Kwak, K.; Fayer, M. D. Probing Dynamics of Complex Molecular Systems with Ultrafast 2D IR Vibrational Echo Spectroscopy. *Phys. Chem. Chem. Phys.* **2007**, *9*, 1533–1549.
- (4) Haleblan, J.; McCrone, W. Pharmaceutical Applications of Polymorphism. *J. Pharm. Sci.* **1969**, *58*, 911–929.
- (5) Haleblan, J. K. Characterization of Habits and Crystalline Modification of Solids and Their Pharmaceutical Applications. *J. Pharm. Sci.* **1975**, *64*, 1269–1288.
- (6) Borcka, L.; Haleblan, J. K. Crystal Polymorphism of Pharmaceuticals. *Acta Pharm. Jugosl.* **1990**, *40*, 71–94.
- (7) Weissenhorn, W.; Dessen, A.; Calder, L.; Harrison, S.; Skehel, J.; Wiley, D. Structural Basis for Membrane Fusion by Enveloped Viruses. *Mol. Membr. Biol.* **1999**, *16*, 3–9.
- (8) Gibbons, D. L.; Vaney, M.-C.; Roussel, A.; Vigouroux, A.; Reilly, B.; Lepault, J.; Kielian, M.; Rey, F. A. Conformational Change and Protein-Protein Interactions of the Fusion Protein of Semliki Forest Virus. *Nature* **2004**, *427*, 320–325.
- (9) Zheng, J.; Kwak, K.; Xie, J.; Fayer, M. D. Ultrafast Carbon-Carbon Single Bond Rotational Isomerization in Room Temperature Solution. *Science* **2006**, *313*, 1951–1955.
- (10) Ernst, R. R.; Bodenhausen, G.; Wokaun, A. *Nuclear Magnetic Resonance in One and Two Dimensions*; Oxford University Press: Oxford, U.K., 1987.
- (11) Bifulco, G.; Dambruoso, P.; Gomez-Paloma, L.; Riccio, R. Determination of Relative Configuration in Organic Compounds by NMR Spectroscopy and Computational Methods. *Chem. Rev.* **2007**, *107*, 3744.
- (12) Chen, H. L.; Bian, H. T.; Li, J. B.; Wen, X. W.; Zheng, J. R. Relative Intermolecular Orientation Probed via Molecular Heat Transport. *J. Phys. Chem. A* **2013**, *117*, 6052–6065.
- (13) Chen, H. L.; Bian, H. T.; Li, J. B.; Wen, X. W.; Zheng, J. R. Ultrafast Multiple-Mode Multiple-Dimensional Vibrational Spectroscopy. *Int. Rev. Phys. Chem.* **2012**, *31*, 469–565.
- (14) Rubtsov, I. V.; Kumar, K.; Hochstrasser, R. M. Dual-Frequency 2D IR Photon Echo of a Hydrogen Bond. *Chem. Phys. Lett.* **2005**, *402*, 439–443.
- (15) Khalil, M.; Demirdoven, N.; Tokmakoff, A. Coherent 2D IR Spectroscopy: Molecular Structure and Dynamics in Solution. *J. Phys. Chem. A* **2003**, *107*, 5258–5279.
- (16) Dong, F.; Miller, R. E. Vibrational Transition Moment Angles in Isolated Biomolecules: A Structural Tool. *Science* **2002**, *298*, 1227–1230.
- (17) Bian, H. T.; Li, J. B.; Wen, X. W.; Sun, Z. G.; Song, J. A.; Zhuang, W.; Zheng, J. R. Mapping Molecular Conformations with Multiple-Mode Two-Dimensional Infrared Spectroscopy. *J. Phys. Chem. A* **2011**, *115*, 3357–3365.
- (18) Bian, H. T.; Li, J. B.; Chen, H. L.; Yuan, K. J.; Wen, X. W.; Li, Y. Q.; Sun, Z. G.; Zheng, J. R. Molecular Conformations and Dynamics on Surfaces of Gold Nanoparticles Probed with Multiple-Mode Multiple-Dimensional Infrared Spectroscopy. *J. Phys. Chem. C* **2012**, *116*, 7913–7924.
- (19) Petersen, P. B.; Tokmakoff, A. Source for Ultrafast Continuum Infrared and Terahertz Radiation. *Opt. Lett.* **2010**, *35*, 1962–1964.
- (20) Calabrese, C.; Stingel, A. M.; Shen, L.; Petersen, P. B. Ultrafast Continuum Mid-Infrared Spectroscopy: Probing the Entire Vibrational Spectrum in a Single Laser Shot with Femtosecond Time Resolution. *Opt. Lett.* **2012**, *37*, 2265–2267.
- (21) Fletton, R. A.; Lancaster, R. W.; Harris, R. K.; Kenwright, A. M.; Packer, K. J.; Waters, D. N.; Yeadon, A. A Comparative Spectroscopic Investigation of Two Polymorphs of 4'-Methyl-2'-nitroacetanilide Using Solid-State Infrared and High-Resolution Solid-State Nuclear Magnetic Resonance Spectroscopy. *J. Chem. Soc., Perkin Trans. 2* **1986**, 1705–1709.
- (22) Wang, J. M.; Wolf, R. M.; Caldwell, J. W.; Kollman, P. A.; Case, D. A. Development and Testing of a General Amber Force Field. *J. Comput. Chem.* **2004**, *25*, 1157–1174.
- (23) Bayly, C. I.; Cieplak, P.; Cornell, W. D.; Kollman, P. A. A Well-Behaved Electrostatic Potential Based Method Using Charge Restraints for Deriving Atomic Charges: The Resp Model. *J. Phys. Chem.* **1993**, *97*, 10269–10280.
- (24) Frisch, M. J.; Trucks, G. W.; Schlegel, H. B.; Scuseria, G. E.; Robb, M. A.; et al. *Gaussian 09*, revision A.02; Gaussian, Inc.: Wallingford, CT, 2009.
- (25) Jorgensen, W. L.; Chandrasekhar, J.; Madura, J. D.; Impey, R. W.; Klein, M. L. Comparison of Simple Potential Functions for Simulating Liquid Water. *J. Chem. Phys.* **1983**, *79*, 926–935.
- (26) Plimpton, S. Fast Parallel Algorithms for Short-Range Molecular-Dynamics. *J. Comput. Phys.* **1995**, *117*, 1–19.
- (27) Shinoda, W.; Shiga, M.; Mikami, M. Rapid estimation of elastic constants by molecular dynamics simulation under constant stress. *Phys. Rev. B* **2004**, *69*, 134103.
- (28) Gattermann, L. Ueber einige Derivate des *m*-Nitro-*p*-Toluidins. *Berichte der deutschen chemischen Gesellschaft* **1885**, *18*, 1482–1488.
- (29) Moore, J. C.; Yeadon, A.; Palmer, R. A. Crystal and Molecular Structures of Two Polymorphs of 4-Methyl-2-nitroacetanilide (MNA). *J. Chem. Cryst.* **1983**, *13*, 279–292.
- (30) Fayer, M. D., Ed. *Ultrafast Infrared and Raman Spectroscopy*; Marcel Dekker, Inc: New York, 2001; Vol. 26.
- (31) Lakowicz, J. *Principles of Fluorescence Spectroscopy*, 3rd ed.; Springer: New York, 2006.
- (32) In addition to the vibrational coupling, the thermal effects induced by the relaxation of NO₂ excitation and the direct vibrational energy transfer from NO₂ to C=O can also produce cross-peaks in Figure 3C.¹³ The signals from these two contributions are waiting-time dependent and also follow eq 1 at very short waiting times before any rotational motion or intermolecular energy dissipation has occurred for a substantial amount.¹²

(33) Bernstein, J. *Polymorphism in Molecular Crystals*; Clarendon Press/International Union of Crystallography: Oxford, U.K., 2002; Vol. 14.

(34) Alarco, P. J.; Abu-Lebdeh, Y.; Abouimrane, A.; Armand, M. The Plastic-Crystalline Phase of Succinonitrile As a Universal Matrix for Solid-State Ionic Conductors. *Nat. Mater.* **2004**, 3, 476–481.

Supporting Information

Vibrational Transition Moment Cross Angles in Condensed Molecules: A

Structural Tool

Hailong Chen¹, Yufan Zhang¹, Jiebo Li¹, Hongtao Bian¹, Hongjun Liu², De-en Jiang²,

Junrong Zheng^{1*}

1 Department of Chemistry, Rice University, Houston, TX 77005, USA

2 Chemical Sciences Division, Oak Ridge National Laboratory, Oak Ridge,
Tennessee 37831, USA

* To whom correspondence should be addressed. E-mail: junrong@rice.edu

Studies on the conformation of methyl group in MNA-W

We used the Vienna Ab Initio Simulation Package (VASP) ^{1,2} to perform DFT calculations with planewave bases and periodic boundary conditions for the MNA crystals. The Perdew-Burke-Erzonhoff (PBE) form of the generalized-gradient approximation (GGA) was chosen for electron exchange and correlation ³. The electron-core interaction was described by the projector-augmented wave (PAW) method ^{4,5} within the frozen-core approximation. A converged kinetic energy cutoff of 400 eV was employed. A converged 4×4×4 Monkhorst-Pack mesh was used to sample the Brillouin zone of the MNA-W crystal whose lattice parameters were fixed at the experimental values during the DFT calculations. The van der Waals interaction was included by the DFT-D2 method of Grimme ⁶. To locate the transition state of the methyl rotation, we employed the climbing-image nudged elastic band (NEB) module implemented in VASP by Henkelman et al. ⁷ Force convergence criterion for both geometry optimization and transition state search was set at 0.025 eV/Å. We used two approaches to estimate the barriers of methyl rotation: a fast method in which we fixed the heavy-than-hydrogen atoms in their XRD-determined positions during geometry optimization and transition-state search; a slow method in which we allowed all atoms to relax. The rotational barriers (1.2 kcal/mol, 0.8kcal/mol) from the slow method are slightly higher than those (0.62 kcal/mol, 0.65 kcal/mol) from the fast method.

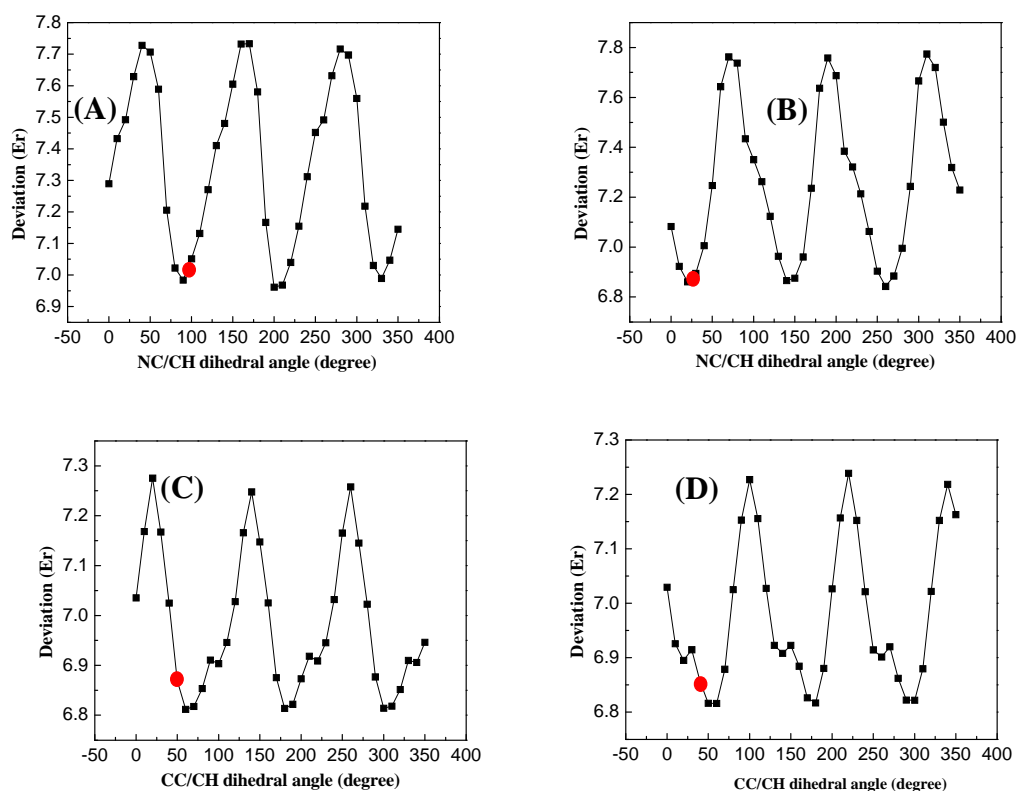


Figure S2. The average difference E_r of the 15 vibrational cross angles between experimental results and calculated results for MNA-W conformations with (A) fixed $(\angle CC/NC, \angle CC/NO) = (50^\circ, 40^\circ)$ and various $\angle NC/CH$ for the amide methyl group; (B) fixed $(\angle CC/NC, \angle CC/NO) = (-50^\circ, -40^\circ)$ and various $\angle NC/CH$ for the amide methyl group; (C) fixed $(\angle CC/NC, \angle CC/NO) = (50^\circ, 40^\circ)$ and various $\angle CC/CH$ for the benzene methyl group; (D) fixed $(\angle CC/NC, \angle CC/NO) = (-50^\circ, -40^\circ)$ and various $\angle CC/CH$ for the benzene methyl group. The red dots indicate the angles with minimum energy used in calculating the dihedral angles for the isolated molecule.

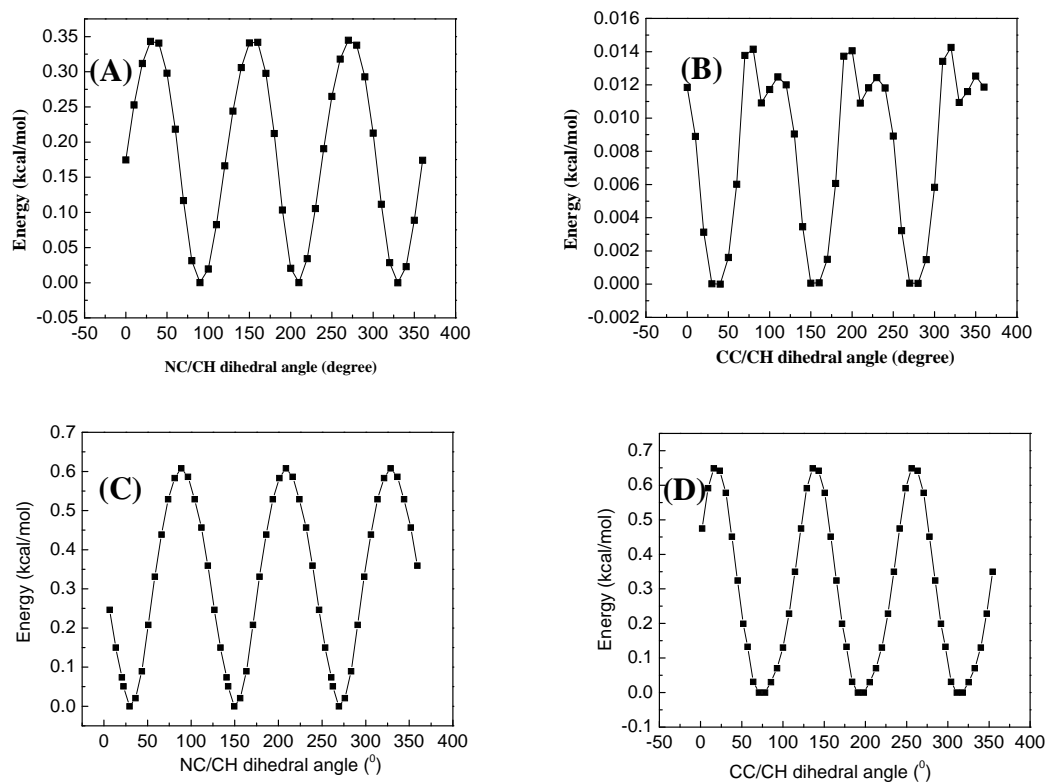


Figure S3. The rotational potential surface of MNA with (A) fixed $(\angle CC/NC, \angle CC/NO) = (50^\circ, 40^\circ)$ and various $\angle NC/CH$ for the amide methyl group for the isolated molecule; (B) fixed $(\angle CC/NC, \angle CC/NO) = (50^\circ, 40^\circ)$ and various $\angle CC/CH$ for the benzene methyl group for the isolated molecule; (C) fixed $(\angle CC/NC, \angle CC/NO) = (-46.4^\circ, -42.6^\circ)$ and various $\angle NC/CH$ for the amide methyl group in MNA-W; (D) fixed $(\angle CC/NC, \angle CC/NO) = (-46.4^\circ, -42.6^\circ)$ and various $\angle CC/CH$ for the benzene methyl group in MNA-W. (C)&(D) are calculated by fixing the heavy-than-H atom positions as determined by XRD.

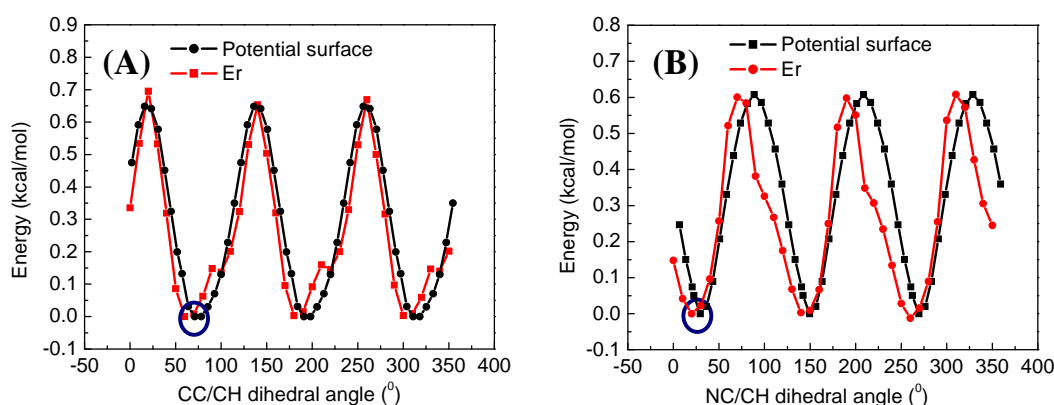


Figure S4. (A) Potential surface (black) at fixed ($\angle CC/NC$, $\angle CC/NO$)= $(-46.4^\circ$, $-42.6^\circ)$ and Er at fixed ($\angle CC/NC$, $\angle CC/NO$)= $(-50^\circ$, $-40^\circ)$ at various $\angle CC/CH$ for the benzene methyl group in MNA-W; (B) Potential surface (black) at fixed ($\angle CC/NC$, $\angle CC/NO$)= $(-46.4^\circ$, $-42.6^\circ)$ and Er at fixed ($\angle CC/NC$, $\angle CC/NO$)= $(-50^\circ$, $-40^\circ)$ at various $\angle NC/CH$ for the amide methyl group in MNA-W. The potential surfaces are from Fig.S3D&C, and the Er data are from fig.S2D&B which are rescaled to match those potential surfaces. The blue circles emphasize that the minima of potential surfaces and Ers are almost identical, indicating that the calculated most probable conformation adopts the most probable dihedral angles experimentally determined by Ers. However, we want to point out that only when most molecules are populated around the energy minimum (case 1), the experimentally determined dihedral angles are very close to the actual angles the most probable conformation adopts. For molecules with many conformations simultaneously populated with significant amounts (case 2), the experimentally determined dihedral angles are just the statistical average of angles of these conformations, which are not necessarily close to those of the most probable

conformation, e.g. for an extreme case where any dihedral angle is equally populated, the average anisotropy can be 0 which gives a vibrational cross angle 54.7° corresponding to only one conformation. For the two methyl groups, the calculated barriers in MNA-W range from 0.6 kcal/mol to 1.2 kcal/mol depending on the calculation methods. The barriers suggest that the situation of the two methyl groups is between case 1 and 2.

FTIR spectra and corresponding assignments of some major absorption peaks

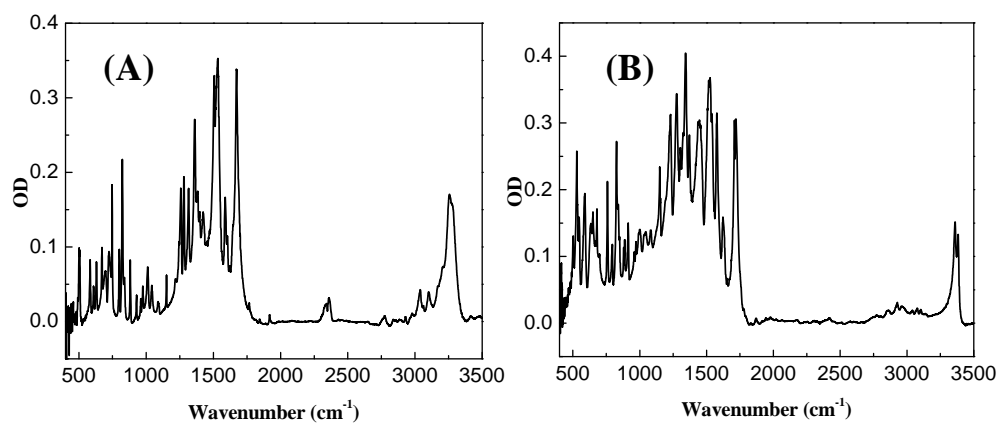


Figure S5. FTIR spectra of (A) MNA-W and (B) MNA-Y. Both of the samples were compressed into KBr pellets for the measurements. The assignment of some major absorption peaks are listed in Table S1.

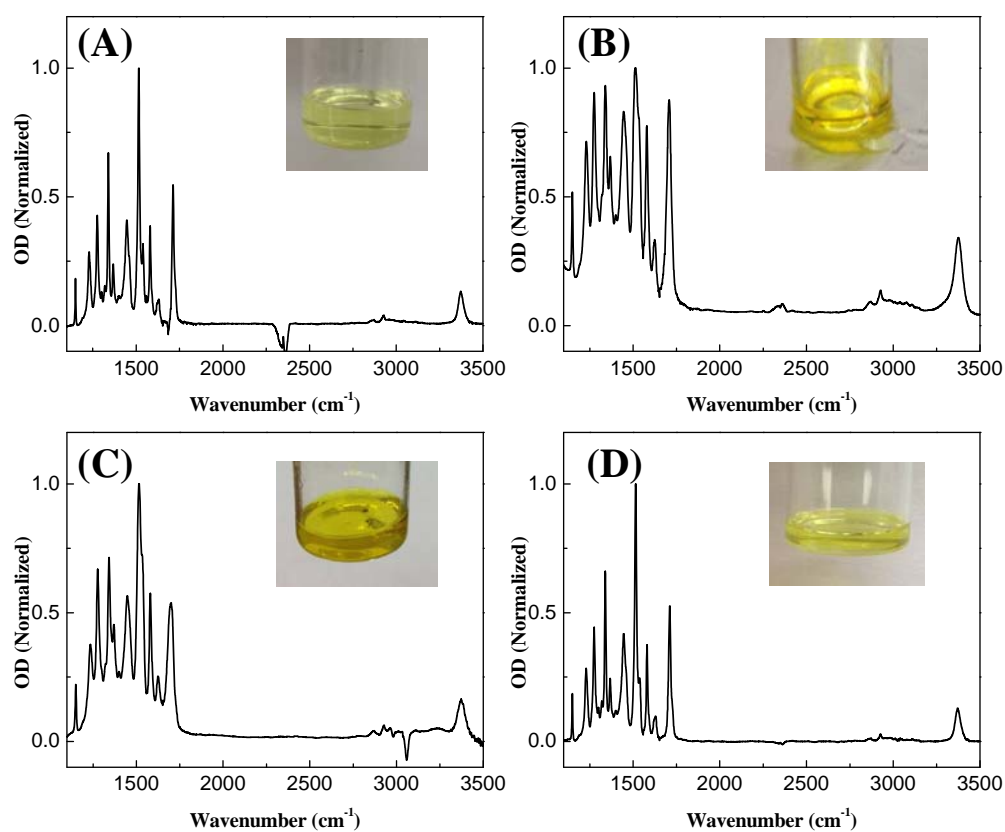


Figure S6. FTIR spectra of the MNA molecules in (A) dilute CCl_4 solution (0.01 M at room temperature), (B) melt form (100°C), (C) saturated aqueous ethanolic solution (2 M at 65°C) and (D) in saturated CCl_4 solution (0.3 M at room temperature) Insets: the appearance of samples. The assignment of some major absorption peaks are listed in Table S2. All samples display a pale yellow color, consistent with the experimental results that all samples have very similar conformations.

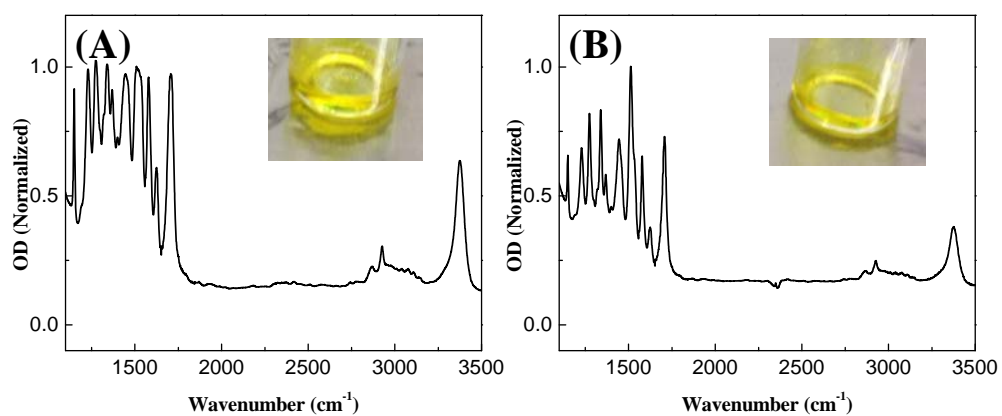


Figure S7. FTIR spectra of MNA molecules melt from (A) MNA-W and (B) MNA-Y.

Insets: the appearance of two polymorphs. Both of them present yellow color. The assignment of some major absorption peaks are listed in Table S2

Table S1. The assignment of the IR peaks (in cm^{-1}) involved in the measurements and calculations for both the white form and the yellow form crystals ⁸. The superscripts 1&2 will be referred in Table S3.

modes	MNA-W	MNA-Y
$\nu(\text{NH})$	3260	3360 ¹ 3383 ²
$\nu(\text{CH arom.})$	3039	—
$\nu(\text{CO})$	1672	1709 ¹ 1720 ²
$\nu_{\text{as}}(\text{NO}_2)$	1533	1541
$\nu_1(\text{C}=\text{C})$	1505	1527
$\nu_s(\text{NO}_2)$	1362	1344
$\nu_2(\text{C}=\text{C})$	1281 ¹ 1258 ²	1277

Table S2. The assignment of the IR peaks (in cm^{-1}) involved in measurements and calculations for different liquid samples.

modes	Sample 1	Sample 2	Melt (white)	Melt (yellow)	Sample 3	Sample 4
$\nu(\text{NH})$	3372	3376	3374	3374	3373	3371
$\nu(\text{CO})$	1712	1708	1707	1707	1701	1712
$\nu_{\text{as}}(\text{NO}_2)$	1539	1534	1538	1537	1535	1538
$\nu_1(\text{C}=\text{C})$	1515	1514	1510	1513	1515	1515
$\nu_s(\text{NO}_2)$	1340	1340	1340	1340	1342	1340
$\nu_2(\text{C}=\text{C})$	1276	1275	1274	1275	1277	1276

Polarization-selective data for all the pairs of coupled vibrational modes of all the samples

Table S3. *Transition dipole moment angles between coupled vibrational modes of the MNA molecules in different phases, all of which are determined from the anisotropy measurements.*

Pair number	Coupled modes	Relative angle (degree)					
		MNA-W	MNA-Y	Sample 1	Sample 2	Sample 3	Sample 4
1	$\nu(\text{NH})/\nu(\text{CO})$	20	—	—	—	—	—
2	$\nu(\text{NH})/\nu_{\text{as}}(\text{NO}_2)$	—	$63^1 65^2$	—	—	—	—
3	$\nu(\text{NH})/\nu_1(\text{C}=\text{C})$	60	$72^1 70^2$	67	66	—	62
4	$\nu(\text{NH})/\nu_{\text{s}}(\text{NO}_2)$	65	$44^1 41^2$	61	53	52	61
5	$\nu(\text{NH})/\nu_2(\text{C}=\text{C})$	$70^1 72^2$	$42^1 41^2$	39	40	35	41
6	$\nu(\text{CH arom.})/\nu_{\text{s}}(\text{NO}_2)$	41	—	—	—	—	—
7	$\nu(\text{CH arom.})/\nu_2(\text{C}=\text{C})$	37^1	—	—	—	—	—
8	$\nu(\text{CO})/\nu_1(\text{C}=\text{C})$	63	$81^1 78^2$	67	—	—	65
9	$\nu(\text{CO})/\nu_{\text{s}}(\text{NO}_2)$	70	$51^1 42^2$	64	56	60	60
10	$\nu(\text{CO})/\nu_2(\text{C}=\text{C})$	86^1	$37^1 39^2$	34	33	32	34
11	$\nu(\text{CO})/\nu_{\text{as}}(\text{NO}_2)$	—	$71^1 68^2$	—	—	—	—
12	$\nu_{\text{as}}(\text{NO}_2)/\nu_{\text{s}}(\text{NO}_2)$	84	73	66	68	66	64
13	$\nu_{\text{as}}(\text{NO}_2)/\nu_2(\text{C}=\text{C})$	$51^1 46^2$	46	—	—	—	—
14	$\nu_1(\text{C}=\text{C})/\nu_{\text{s}}(\text{NO}_2)$	70	50	47	51	51	49
15	$\nu_1(\text{C}=\text{C})/\nu_2(\text{C}=\text{C})$	26^1	54	42	41	38	41

Table S4. *Scaling factors for the multiple-mode 2D IR spectrum shown in Fig. 2A.*

Region	Dividing factor ($\times 10^{-5}$)	Region	Dividing factor ($\times 10^{-5}$)
Pump 1200-1420 cm^{-1} Probe 1240-1295 cm^{-1}	1.0	Pump 1200-1420 cm^{-1} Probe 1295-1400 cm^{-1}	1.5
Pump 1200-1420 cm^{-1} Probe 1400-1560 cm^{-1}	8.6	Pump 1200-1420 cm^{-1} Probe 1560-1720 cm^{-1}	4.1
Pump 1440-1740 cm^{-1} Probe 1240-1295 cm^{-1}	0.7	Pump 1440-1740 cm^{-1} Probe 1295-1400 cm^{-1}	3.4
Pump 1440-1740 cm^{-1} Probe 1400-1560 cm^{-1}	15.9	Pump 1440-1740 cm^{-1} Probe 1560-1720 cm^{-1}	5.9
Pump 3000-3340 cm^{-1} Probe 1240-1295 cm^{-1}	0.7	Pump 3000-3340 cm^{-1} Probe 1295-1400 cm^{-1}	3.0
Pump 3000-3340 cm^{-1} Probe 1400-1560 cm^{-1}	13.4	Pump 3000-3340 cm^{-1} Probe 1560-1720 cm^{-1}	14.3

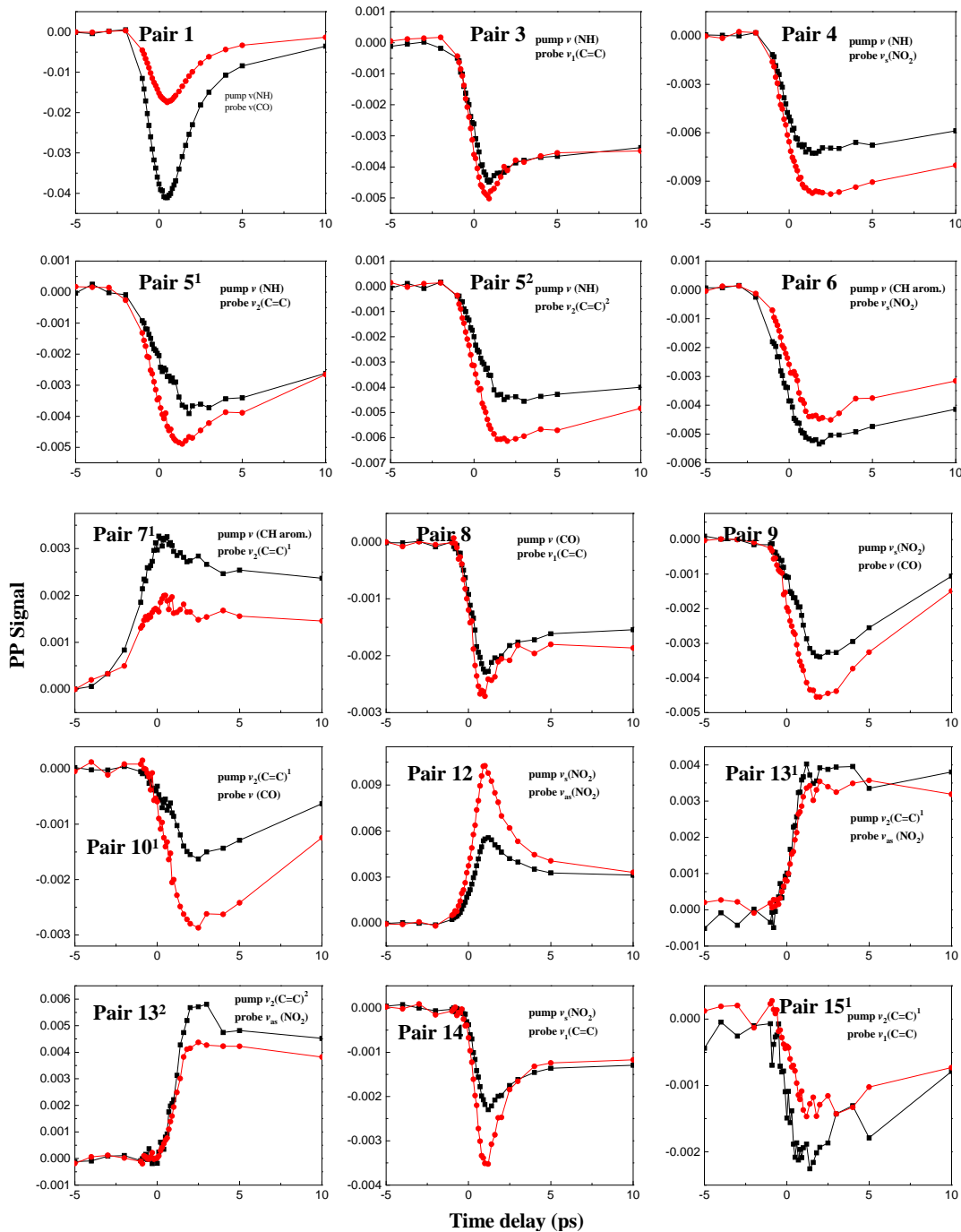
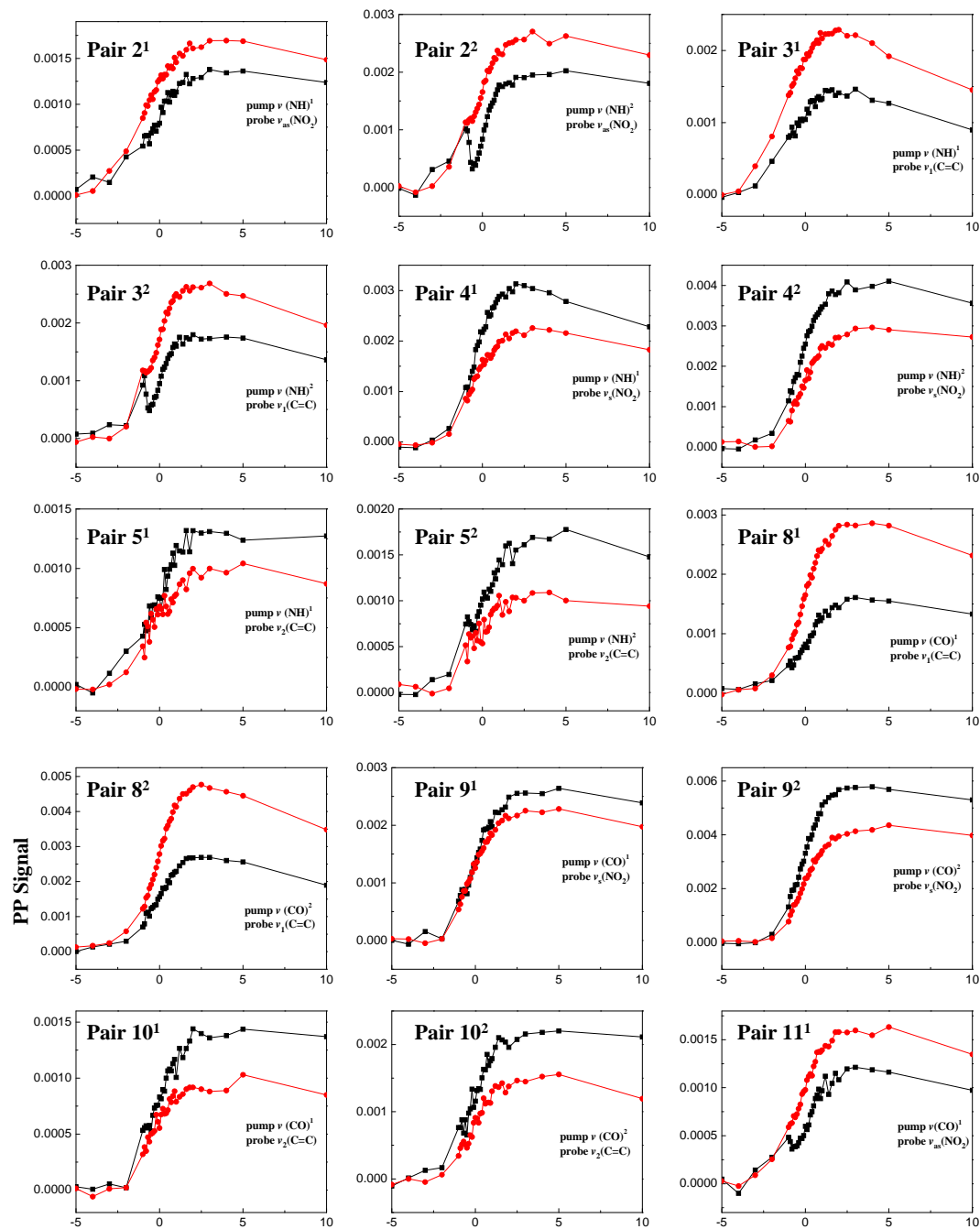


Figure S8. Polarization selective pump/probe data for all the measured pairs of coupled vibrational modes of MNA-W. In addition to the vibrational coupling mentioned in the main text, the thermal effects induced by the relaxation of NO_2 excitation and the direct vibrational energy transfer from NO_2 to $\text{C}=\text{O}$ can also produce cross peaks in fig.3C⁹. The signals from these two contributions are

waiting-time dependent and also follow eq.1 at very short waiting times before any rotational motion or intermolecular energy dissipation has occurred by a substantial amount¹⁰.



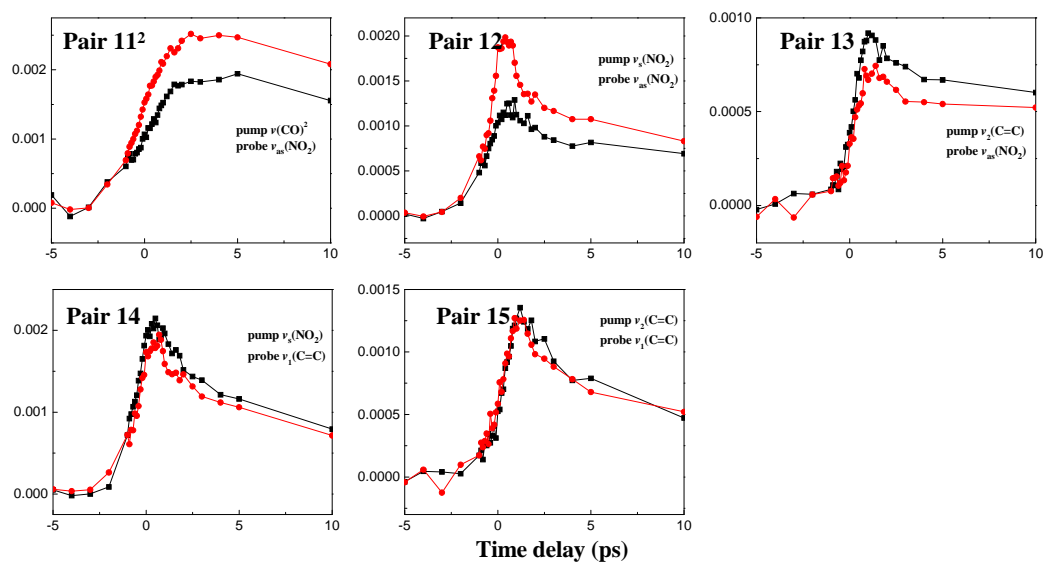


Figure S9. Polarization selective pump/probe data for all the measured pairs of coupled vibrational modes of MNA-Y.

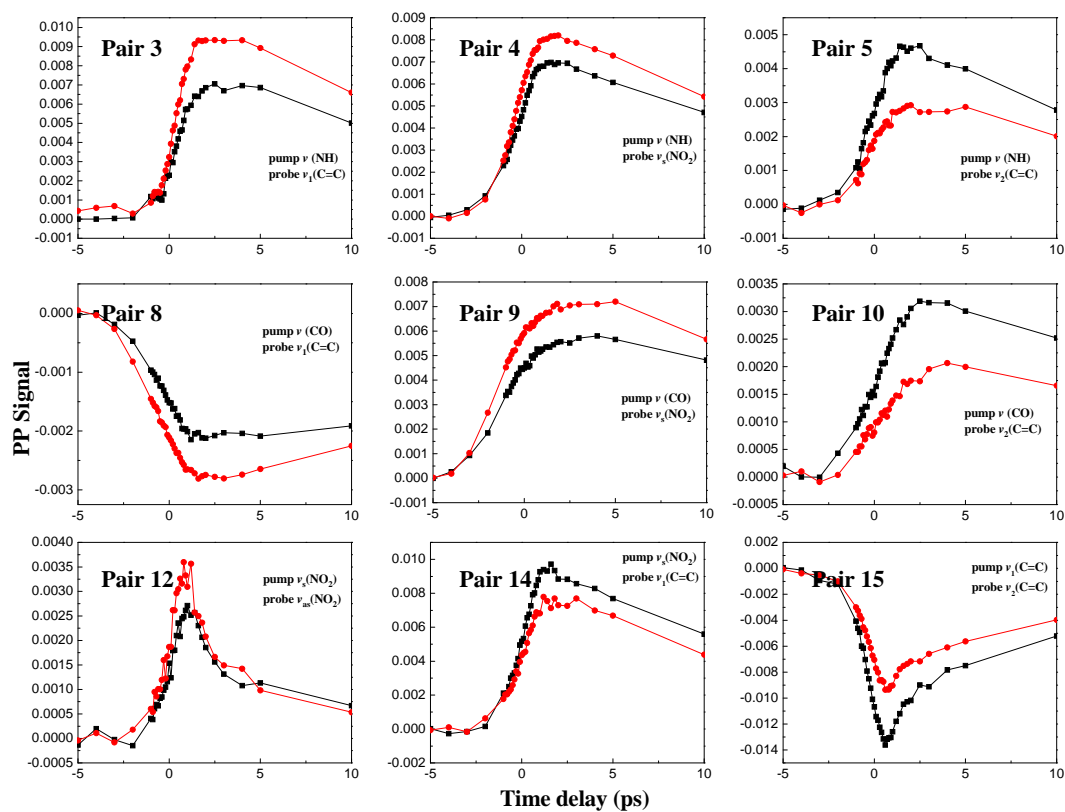


Figure S10. Polarization selective pump/probe data for all the measured pairs of coupled vibrational modes of MNA molecules in dilute CCl₄ solution (0.01 M at room temperature, Sample 1).

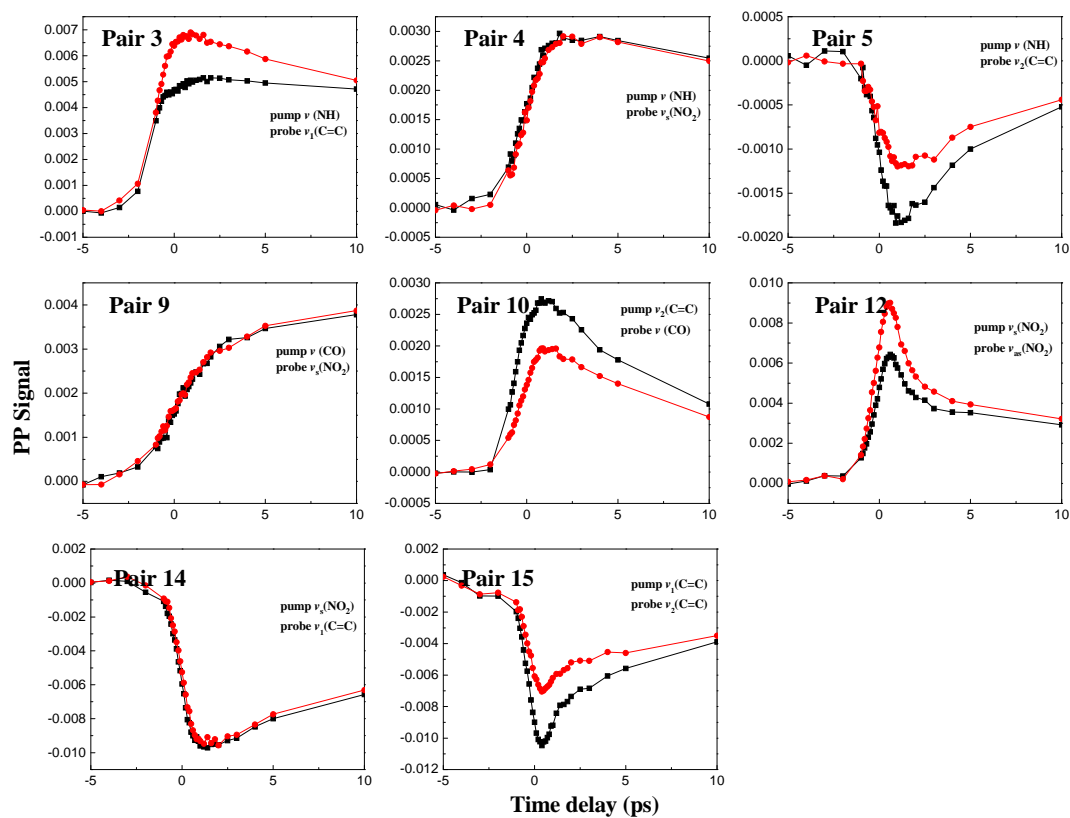


Figure S11. Polarization selective pump/probe data for all the measured pairs of coupled vibrational modes of MNA molecules in melt form (100°C, from the sample that purchased, Sample 2).

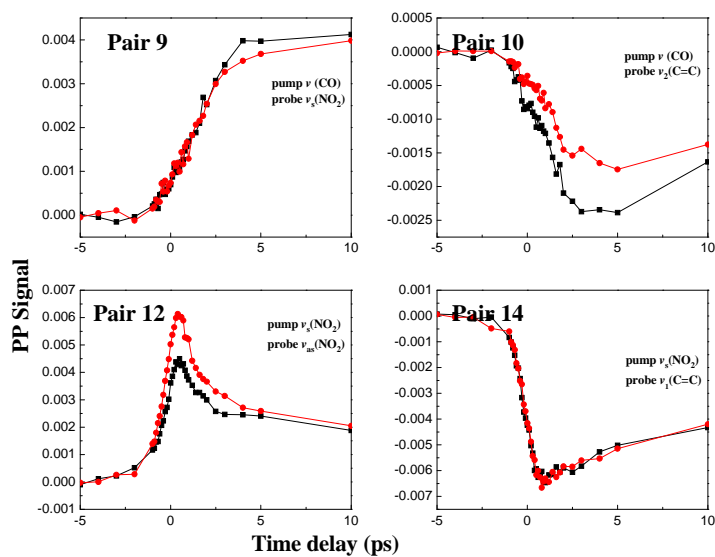


Figure S12. Polarization selective pump/probe data for all the measured pairs of coupled vibrational modes of MNA molecules in melt form (100°C, from the white sample).

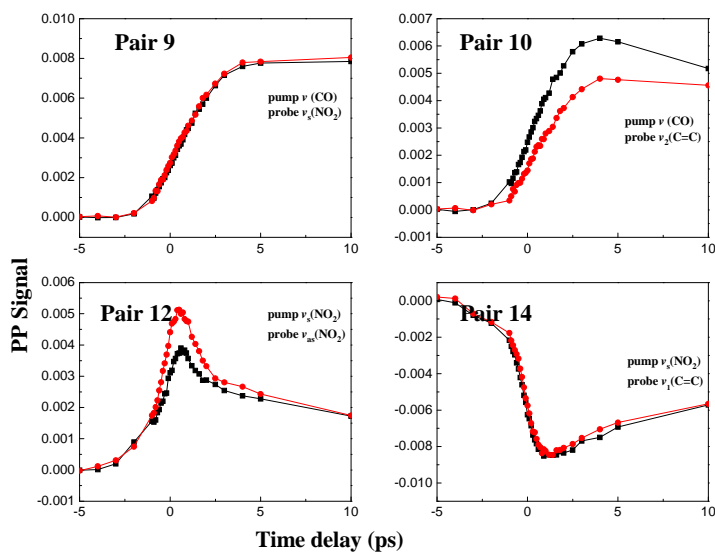


Figure S13. Polarization selective pump/probe data for all the measured pairs of coupled vibrational modes of MNA molecules in melt form (100°C, from the yellow sample).

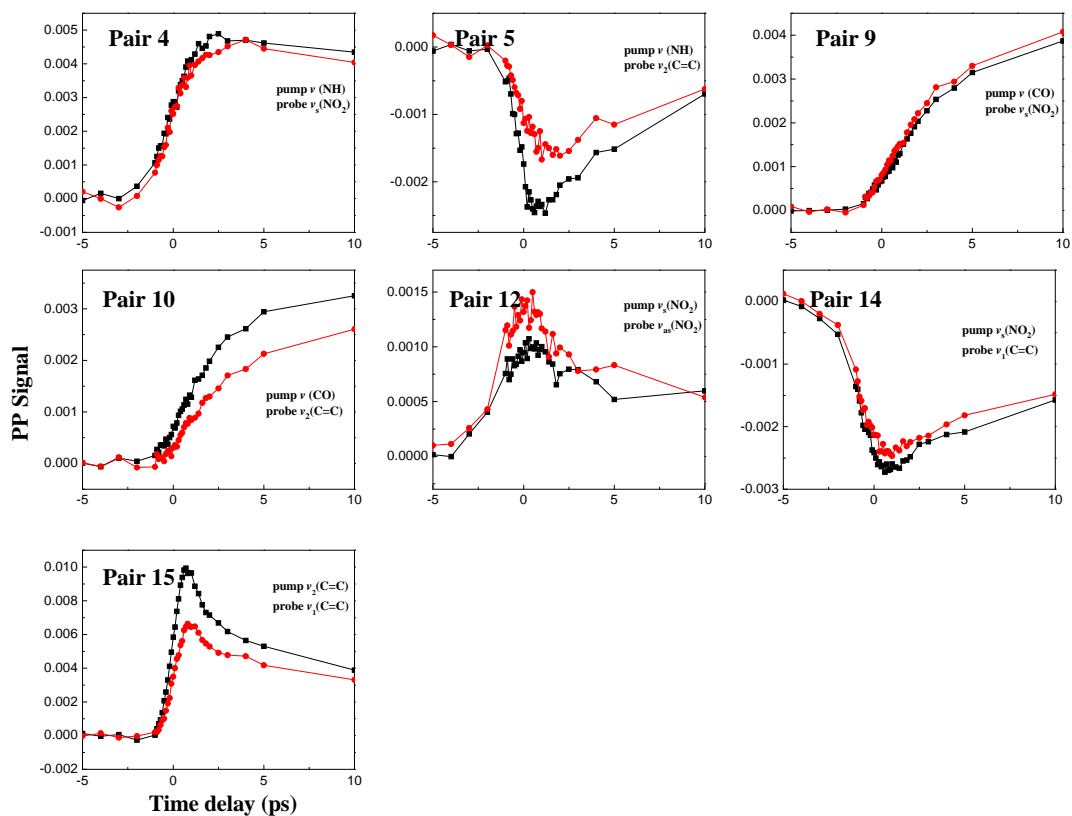


Figure S14. Polarization selective pump/probe data for all the measured pairs of coupled vibrational modes of MNA molecules in saturated aqueous ethanolic solution (2 M at 65°C, Sample 3).

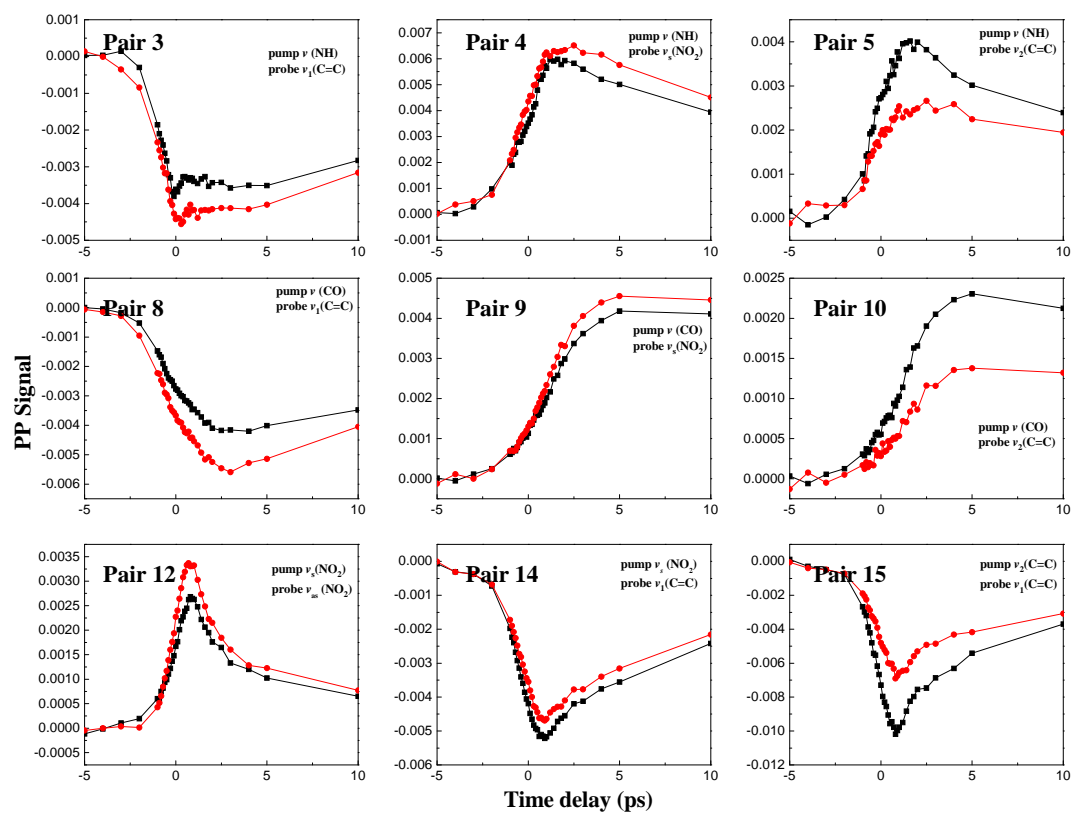


Figure S15. Polarization selective pump/probe data for all the measured pairs of coupled vibrational modes of MNA molecules in saturated CCl_4 solution (0.3 M at room temperature, Sample 4).

Dependence of vibrational cross angles on the conformation

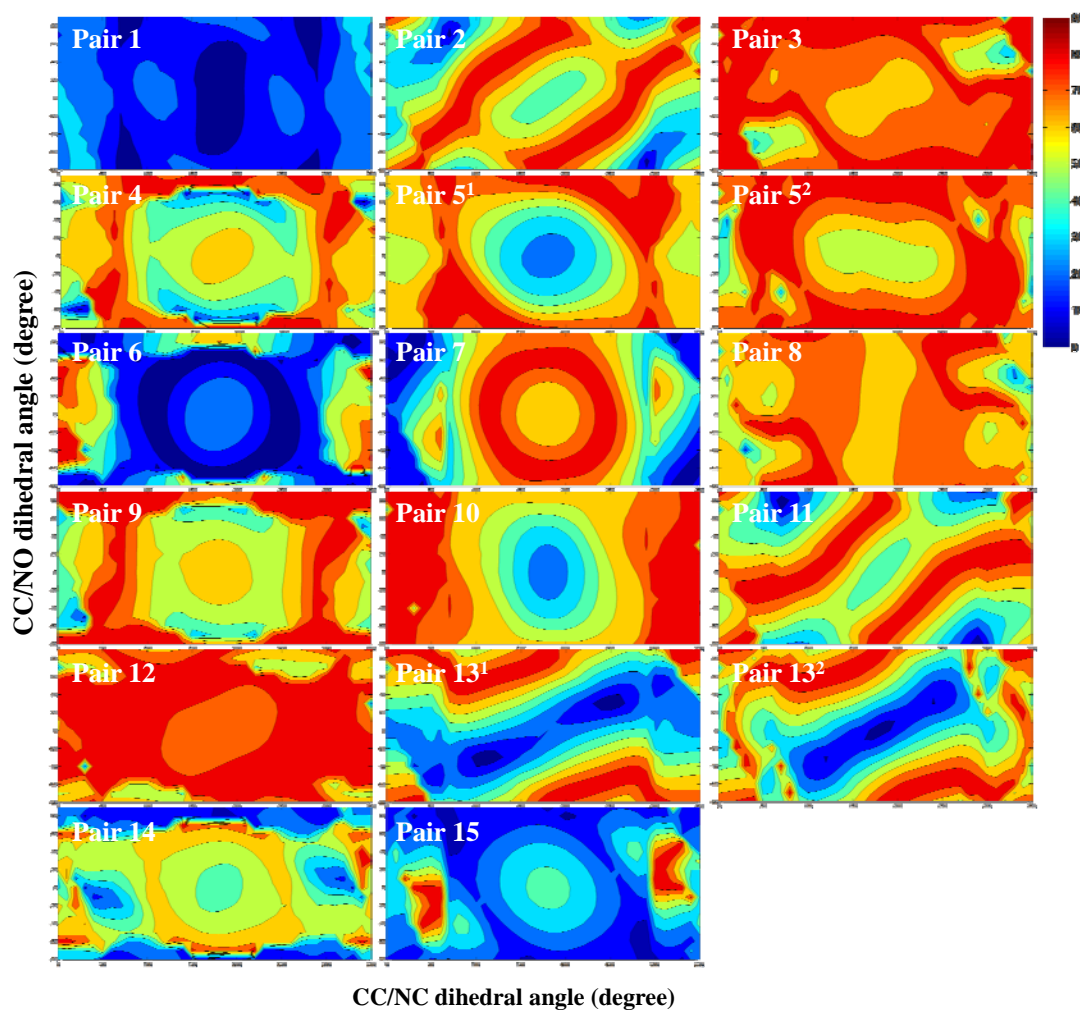


Figure S16. All involved calculated vibrational cross angles of different MNA conformations with various $\angle CC/NO$ and $\angle CC/NC$ dihedral angles. The z-axis (intensity) is the vibrational cross angle θ . It can be seen that the correlations between the vibrational cross angles and the dihedral angles of different modes are generally different.

Dependence of the average difference Er on the conformation

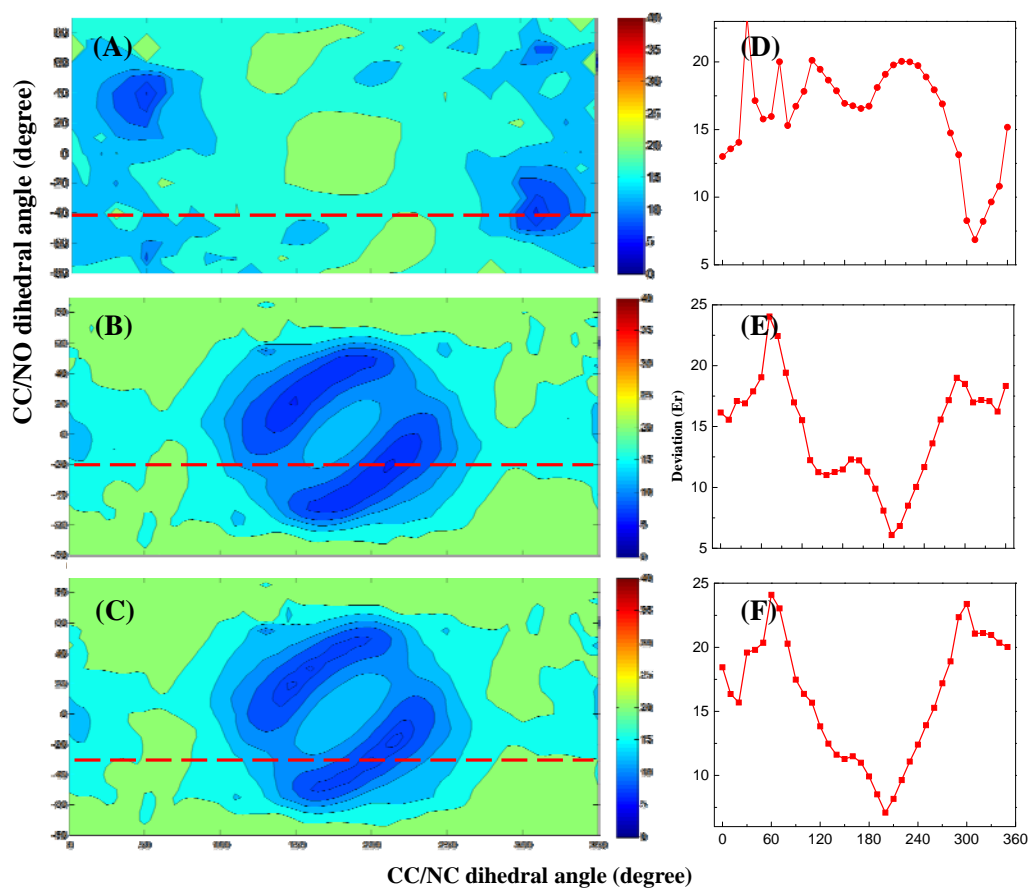


Figure S17. The average difference Er between the experimental and calculated vibrational cross angles of MNA conformations with different $\angle CC/NO$ and $\angle CC/NC$ dihedral angles for (A) MNA-W, (B) MNA-Y1, and (C) MNA-Y2, which are the same as those in fig. 3A-C. (D) A slice cut along $\angle CC/NO = -40^\circ$ of fig. S17A. (E) A slice cut along $\angle CC/NO = -20^\circ$ of fig. S17B. (F) A slice cut along $\angle CC/NO = -30^\circ$ of fig. S17C. The minima of Er are clearly visible in fig. (D)~(F).

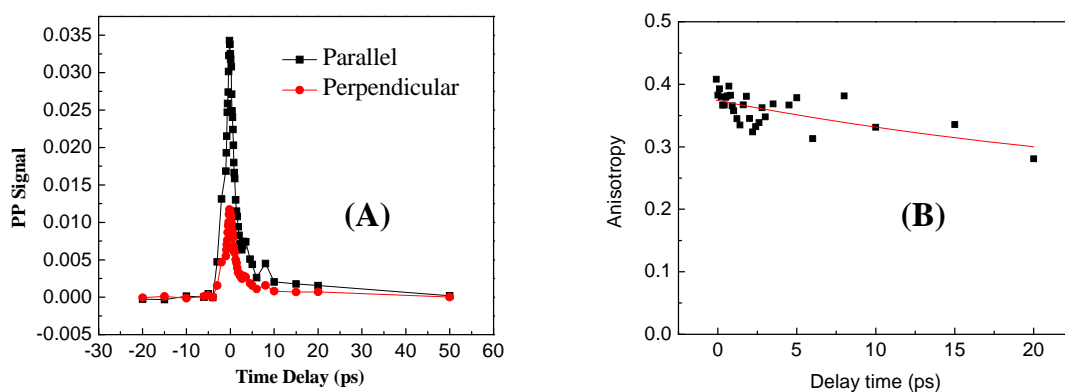


Figure S18. (A) Pump/probe data of exciting the C=O stretch 0-1 transition in the dilute MNA CCl_4 solution. (B) The anisotropy data from the pump/probe measurements. Dots are data, and the line is a fit with a single exponential with a time constant 33ps. The anisotropy values within the first 1ps are almost unchanged because of the slow rotation. The results indicate that the vibrational cross angle measurements are hardly affected by the molecular rotation.

Comparing the experimental and calculated vibrational frequencies

We tested the possibility of determining molecular conformations by comparing the values of experimental and calculated vibrational frequencies. The procedure is very similar to that for the vibrational cross angles:

$$Er' = \frac{\sum_{i=1}^n |F_i^C - F_i^E|}{n}, \quad (S1)$$

where F_i^C is the calculated vibrational frequency (multiplied by a scaling factor 0.96) of i^{th} normal modes of a molecular conformation with a pair values (x_i, y_i) of dihedral angles $(\angle CC/NC, \angle CC/NO)$. F_i^E is the experimental vibrational frequency of the i^{th} normal modes, and n is the number of all used normal modes. Similarly, the dihedral angle values (x_m, y_m) of the conformation giving the smallest Er' are supposed to be the most probable angles that the molecular conformation in the sample adopts. However, as shown in fig. S19, no clear correlation between the frequency and the molecular conformation can be found, different from the vibrational cross angle as demonstrated in this work. This is probably mainly because the vibrational frequencies are affected by not only the molecular conformations, but also combination bands and overtones which are difficult to compute with high precision. The influences of combination bands and overtones on vibrational cross angles are very slight because the transition dipole moments of the normal modes from which the experimental signal of vibrational cross angles mainly comes are much larger than those of the high order transitions. Intermolecular interactions can be another reason. It is well known the vibrational frequency can be significantly shifted by intermolecular interactions, e.g. H-bonds. The

vibrational cross angle is probably less affected, as it is mainly caused by intramolecular coupling.

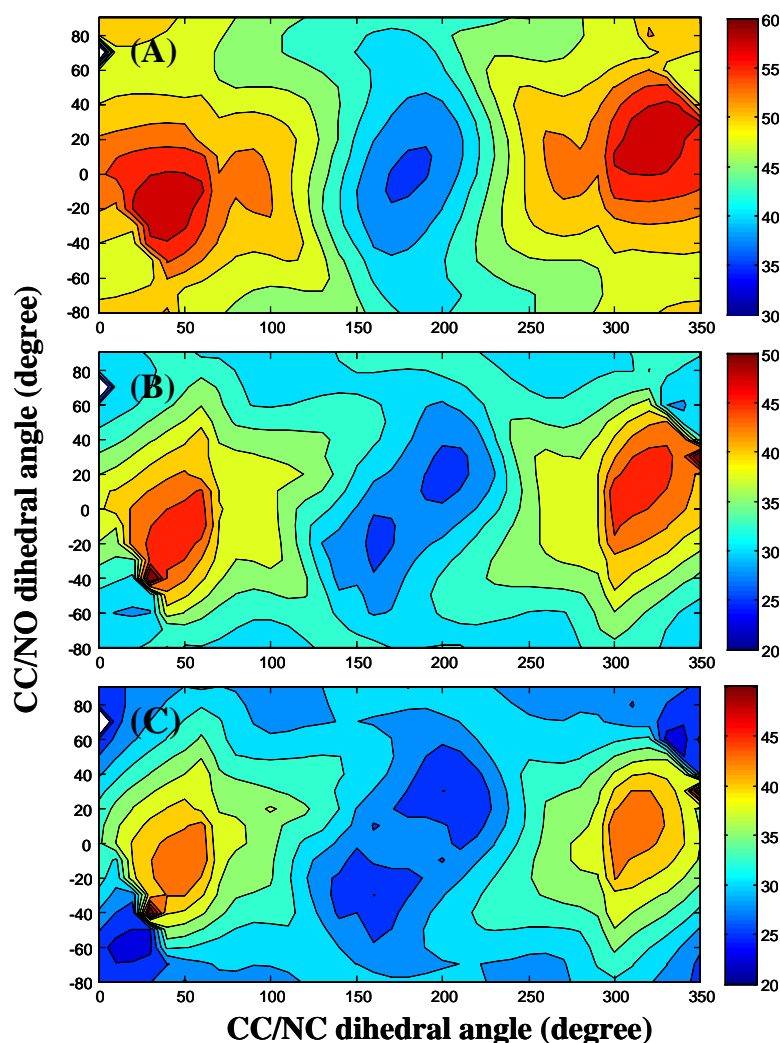


Figure S19. The average difference Er' between the experimental and calculated vibrational frequencies of MNA conformations with different $\angle CC/NO$ and $\angle CC/NC$ dihedral angles for (A) MNA-W, (B) MNA-Y1, and (C) MNA-Y2. The z-axis is the amplitude of Er' . 7 normal modes were employed for MNA-W, which are $\nu(NH)$, $\nu(CH\text{ arom.})$, $\nu(CO)$, $\nu(C=C)$ (at 1588 cm^{-1}), $\nu_{as}(NO_2)$, $\nu_l(C=C)$ and $\nu_s(NO_2)$. For MNA-Y1&Y2, 6 normal modes were employed which are $\nu(NH)$, $\nu(CO)$, $\nu(C=C)$ (at 1578 cm^{-1}), $\nu_{as}(NO_2)$, $\nu_l(C=C)$ and $\nu_s(NO_2)$. The results show that no clear correlation between the frequency and the molecular conformation can be found,

different from the vibrational cross angle as demonstrated in this work.

Reference

- (1) Kresse, G.; Furthmüller, J. Efficient iterative schemes for ab initio total-energy calculations using a plane-wave basis set. *Physical Review B: Condensed Matter* **1996**, *54*, pp.11169-11186.
- (2) Kresse, G.; Furthmüller, J. Efficiency of ab-initio total energy calculations for metals and semiconductors using a plane-wave basis set. *Computational Materials Science* **1996**, *6*, pp.15-50.
- (3) Perdew, J. P.; Burke, K.; Ernzerhof, M. Generalized gradient approximation made simple. *Phys. Rev. Lett.* **1996**, *77*, pp.3865-3868.
- (4) Blöchl, P. E. Projector augmented-wave method. *Physical Review B* **1994**, *50*, pp.17953-79.
- (5) Kresse, G.; Joubert, D. From ultrasoft pseudopotentials to the projector augmented-wave method. *Physical Review B: Condensed Matter and Materials Physics* **1999**, *59*, pp.1758-1775.
- (6) Grimme, S. Semiempirical GGA-type density functional constructed with a long-range dispersion correction. *Journal of Computational Chemistry* **2006**, *27*, pp.1787-1799.
- (7) Henkelman, G.; Uberuaga, B. P.; Jonsson, H. A climbing image nudged elastic band method for finding saddle points and minimum energy paths. *Journal of Chemical Physics* **2000**, *113*, pp.9901-9904.
- (8) Fletton, R. A.; Lancaster, R. W.; Harris, R. K.; Kenwright, A. M.; Packer, K. J.; Waters, D. N.; Yeadon, A. A comparative spectroscopic investigation of two polymorphs of 4'-methyl-2'-nitroacetanilide using solid-state infrared and high-resolution solid-state nuclear magnetic resonance spectroscopy. *Journal of the Chemical Society, Perkin Transactions 2: Physical Organic Chemistry* **1986**, pp.1705-1709.
- (9) Chen, H. L.; Bian, H. T.; Li, J. B.; Wen, X. W.; Zheng, J. R. Ultrafast multiple-mode multiple-dimensional vibrational spectroscopy. *Inter. Rev. Phys. Chem.* **2012**, *31*, pp.469-565.
- (10) Chen, H. L.; Bian, H. T.; Li, J. B.; Wen, X. W.; Zheng, J. R. Relative intermolecular orientation probed via molecular heat transport. *J. Phys. Chem. A.* **2013**, DOI: 10.1021/jp312604v.